Fall 2011

Density determination of tristructural-isotropic nuclear fuel using multiple projection x-ray radiography

Frank Angelo Strantz

Department:

DENSITY DETERMINATION OF TRISTRUCTURAL-ISOTROPIC NUCLEAR FUEL USING MULTIPLE PROJECTION X-RAY RADIOGRAPHY

by

FRANK ANGELO STRANTZ

A THESIS

Presented to the Faculty of the Graduate School of the

MISSOURI UNIVERSITY OF SCIENCE AND TECHNOLOGY

In Partial Fulfillment of the Requirements for the Degree

MASTER OF SCIENCE IN NUCLEAR ENGINEERING

2011

Approved by:

Hyoung Koo Lee, Advisor
Carlos H. Castaño
Shoaib Usman

ABSTRACT

Effective methods of enhancing the safety and efficiency of the nuclear power industry embolden its perception and economic viability. Fuel reliability is an essential component of the prosperity of next generation high temperature reactors; as such, an equally dependable quality control method is mandatory. Tristructural-isotropic (TRISO) fuel, the fuel developed for use in these reactors, utilizes density measurement of coating layers as a standard for quality control. Common methods of measuring density, such as sink-float and ceramography are destructive, and as such generate radioactive waste, take a relatively long time to prepare samples, rely on a low sampling rate to be economical, and destroy otherwise usable samples.

An alternative method which is non-destructive, quick, robust, and potentially automated has been developed by utilizing typical x-ray radiography. Simulated images and actual radiographs were used to test the method. The simulated results indicated that the method has high tolerance for image noise. Additional tests were performed for voltage fluctuations, errors in the photon energy distribution, and radii measurement perturbations. Experiments were performed with a TRISO fuel phantom and the calculated density results were found to be in agreement with actual values. Implications of the developed testing method include more stringent quality control of fuel at a rapid inspection rate, minimization of fission product release from fuel, and ultimately, increased reactor efficiency.

ACKNOWLEDGMENTS

I am greatly thankful for the constant support and assistance from my advisor, Dr. Hyoung Koo Lee. His wealth of knowledge pertaining to nuclear and imaging physics have proved essential in making this work possible. He provided me with the freedom to pursue my own research ideas and guided me when I needed direction.

I would also like to thank the members of my advisory committee, Dr. Carlos H. Castaño, and Dr. Shoaib Usman, for their guidance and support. From when I was an undergraduate at Missouri S&T to now, they have continually helped to build the nuclear engineering knowledge I possess today. The Missouri S&T reactor staff played a vital role in this project by helping me with x-ray radiography experiments. I thank them for their constructive input and patients which helped immensely.

The assistance and information provided by Dr. Andrew Kercher and his colleagues from Oak Ridge National Laboratory related to TRISO fuel was indispensible in helping me learn more about radiography and the fuel particles. I would like to thank the Nuclear Regulatory Commission Faculty Development Fund for financial assistance in buying materials for the phantom fuel particle.

Finally, I would like to recognize the support of my family and Sarah Arcuri. Their unyielding support strongly motivated me, making the difficult parts of this journey much easier.

TABLE OF CONTENTS

LIST OF ILLUSTRATIONS

LIST OF TABLES

NOMENCLATURE

Symbols	Description
I	Final intensity
I_0	Initial intensity
t	Photon path length
μ	Linear attenuation coefficient
μ/ρ	Mass attenuation coefficient
ρ	Density
θ	Inclination angle
Φ	Azimuth angle
r	Radius
H	Component of radius projected onto the x-z axis
L	Length between the source and a point on the surface of a fuel layer
w	Free parameter used in line equations
n	Number of energy bins
c	Constant of proportionality between pixel value and absorbed energy
P	Pixel value
E	Energy
N	Number of photons
B	Bright image
D	Dark image
R	Raw radiograph image
F	Flat-field corrected image

Subscripts	Description
1	Refers to the TRISO fuel kernel
2	Refers to the TRISO fuel buffer layer
3	Refers to the TRISO fuel IPyC layer
4	Refers to the TRISO fuel SiC layer
5	Refers to the TRISO fuel OPyC layer

BG	Refers to the background of an image
D	Refers to the detector
O	Refers to the object being imaged
S	Refers to the source
in	Refers to inside
out	Refers to outside
max	Refers to maximum value

Acronyms	**Description**
AGR	Advanced Gas Reactor
AVR	Arbeitsmeinscaft Versuchsreaktoren
BISO	Bistructural-Isotropic
BWR	Boiling Water Reactor
DOE	Department of Energy
GT-MHR	Gas Turbine-Modular Helium Reactor
HTGR	High Temperature Gas Reactor
HTR-10	High Temperature Reactor (10 MWt)
HTTR	High Temperature Test Reactor
IAEA	International Atomic Energy Agency
IIDC	Irradiation-Induced Dimensional Change
IPyC	Inner Pyrocarbon
MCNP	Monte Carlo N-Particle
OPyC	Outer Pyrocarbon
PWR	Pressurized Water Reactor
SiC	Silicon Carbide
TRISO	Tristructural-Isotropic
VHTR	Very High Temperature Reactor

1. INTRODUCTION

1.1. OBJECTIVE AND SCOPE

The designs of operating commercial nuclear reactors in the United States all stem from 1960s technology. Many of these reactors have been running for more time than they were initially licensed to via operating life extensions. In the next decades, the finite life of these reactors coupled with an increasing electricity demand will necessitate construction of additional plants. In addition to expanding the current nuclear fleet with traditional reactors, a new generation of reactors is being researched. This combination of efforts is a step toward meeting future energy needs and emboldening public perception of the nuclear industry.

Several next generation reactor designs have been investigated. In terms of safety, efficiency and supplemental benefits, such as hydrogen production, a type of High Temperature Gas Reactor (HTGR) called the Very High Temperature Reactor (VHTR) is the favored next generation design for the Generation IV International Forum, an international group for investigating future nuclear power technologies [1]. As opposed to the current fleet of Pressurized Water Reactors (PWRs) and Boiling Water Reactors (BWRs) that globally dominate the nuclear power generation fleet, the HTGR design relies on passive safety features. These passive safety features are inherent in the design, which boasts a high heat capacity and a specific core loading to ensure temperature increases occur slowly and a safe maximum fuel temperature exists [2]. Experiments at the German HTGR, Arbeitsgemeinschaft Versuchsreaktor (AVR), have shown that even with the failure of control and cooling systems, the reactor is stabilized by the inherent negative temperature coefficient. Operating at a higher temperature also improves reactor efficiency. The outlet temperature of the AVR is 950 degrees Celsius. This coincides with the International Atomic Energy Agency (IAEA) design goals of the HTGR reactor materials withstanding 950 degrees Celsius during normal operation and 1600 degrees Celsius during accident scenarios [3]. The HTGR has not been commercially deployed for political, economic, and some technical issues. Research is ongoing.

One prominent subject of HTGR research is fuel. As the coolant medium and operating conditions of the HTGR are dissimilar to those of current nuclear reactors, a different fuel design is utilized. The efficacy of this fuel, known as Tristructural-Isotropic (TRISO) fuel, is fundamental to the viability of the HTGR. Unlike the current fleet of reactors which have large containment vessels surrounding the core for structural and radiation related concerns, the fuel particles are the basis for radiation containment in the HTGR. As such, performance of these fuel particles largely determines the value of the HTGR reactor design. In fact, passive safety features, contamination prevention, operating efficiency, and ease of depository storage all depend on properly manufactured fuel [2]. Such is the importance that the highest priority of the United States and German fuel development efforts is reducing initial defects in the fuel [1]. Unfortunately, the manufacturing process of these particles is susceptible to introducing a variety of fuel defects. Reactor designs, such as the Modular Helium Reactor design, require fifteen billion TRISO particles in a core loading. To handle such a production volume and ensure the reactors have a sufficiently low fuel defect fraction, a dependable quality control method is required [4].

Presented is a new method for analyzing several TRISO fuel quality control parameters utilizing x-ray radiography. The algorithm measures fuel coating layer thicknesses, calculates their densities, and can be used to detect missing layers or abnormal shapes. The algorithm can be used with unfinished and completed TRISO fuel particles. If TRISO fuel was being manufactured at a rate to support commercial power generation, an inspection rate of 200 TRISO particles per second would be required for 100 percent inspection [4]. With parallel inspection lines and expansion of this algorithm to analyze several fuel particles in a single radiograph, such inspection rates may be possible.

1.2. TRISO FUEL

1.2.1. Description. TRISO fuel is a layered fuel design consisting of a spherical fissile or fertile kernel wrapped in four isotropic coating layers. Among the four layers, there are three different structures, hence the name. The TRISO fuel design is the third in

a series of coated fuel pellet designs. First, a laminar design was developed in which a single, anisotropic pyrocarbon layer surrounded a fuel kernel [1]. A second design was produced and called Bistructural-Isotropic (BISO) fuel. BISO fuel boasted both a low density pyrocarbon layer and a high density pyrocarbon layer around the fuel kernel. Unlike its predecessor, the BISO design is capable of retaining fission products without cracking under pressure buildup thanks to voids in the low density layer. Further improvement to layered fuel designs led to the modern TRISO fuel, which incorporates a third structure, silicon carbide (SiC), and is the standard fuel among all HTGRs today.

A variety of nations have invested in programs related to the design or manufacture of TRISO fuel. Among these are Argentina, Brazil, Canada, China, France, Germany, Japan, the Republic of Korea, the Republic of South Africa, Russia, Switzerland, the United Kingdom, and the United States. Among these nations, several different fuel compositions have been adopted as standards. The coating layer materials are all consistent, however.

There are fissile and fertile TRISO fuel designs. General Atomics and Oak Ridge National Laboratory are the two producers of TRISO fuel in the United States [5]. General Atomics produced fuel in large quantities in order to load Peach Bottom 1, Fort St. Vrain, and the Gas Turbine-Modular Helium Reactor (GT-MHR) [4]. Oak Ridge National Laboratory produces fuel for design and analysis research purposes.

1.2.1.1 Kernel. Fission events and energy production occur in the kernel of the fuel. The kernel is designed to be several hundred microns in diameter; the Advanced Gas Reactor (AGR) program in the United States uses a 425 micron fuel diameter [6]. The kernel material varies depending on design needs. Both fissile and fertile kernel designs exist, the most common materials for which are uranium and thorium, respectively. The uranium and thorium are utilized in the form of carbides, oxides, or a combination of the two. The German AVR, Japanese High Temperature Test Reactor (HTTR), and Chinese 10 MWt High Temperature Reactor (HTR-10) all use UO_2 kernels [6]. Both UC_2 and UO_2 kernels have advantages and downfalls. Mitigating disadvantages of both designs is the UCO kernel, which is composed of distinct UC_2 and UO_2 phases [1,6,7]. This kernel lessens common issues among TRISO fuel such as kernel migration, CO production, and rare earth element attack [1,6]. As such, it was chosen as the

reference design for the Department of Energy (DOE) HTGR development program [1]. The production of the kernels is through the sol-gel method, involving a series of chemical reactions, washing, drying, calcination, and sintering [5,7,8].

1.2.1.2 Buffer. The first layer surrounding the kernel of TRISO fuel is a porous buffer layer made of pyrocarbon. The buffer layer is the thickest of the coating layers, measuring from 50 to 100 microns thick depending on the fuel type. It is responsible for absorbing fission recoils, containing fission gases, and accommodating swelling of the kernel [1,6]. By containing fission products, radiation release is controlled and pressure is managed.

Fluidized bed chemical vapor deposition is used to apply all of the coating layers. This process involves placing a batch of particles in a coating machine which operates at high temperatures and has a gas mixture pumped through. Two gases make up the mixture, one that is decomposed and slowly builds the coating layer and one that is inert and acts as a working fluid. During fluidized bed chemical vapor deposition, the properties of the deposited layer are dependent on the deposition temperature and gas mixture [9]. For the buffer, this process is done at 1250 to 1300 degrees Celsius with an argon and acetylene (C_2H_4) gas mixture, the ratio and quantity of which is set to control coating characteristics such as the coating rate and microstructure formation [8].

1.2.1.3 Inner pyrocarbon. Over the buffer layer a denser pyrocarbon layer is chemically deposited, known as the inner pyrocarbon (IPyC) layer. Similarly to the buffer layer, the IPyC layer is responsible for containing fission products. More importantly it acts as protection for the kernel during the deposition process of the next coating layer which involves chlorine that could potentially react with the kernel to form undesirable uranium chlorides [6].

The chemical vapor deposition gas mixture used to deposit the IPyC layer is an argon, acetylene, and propylene (C_3H_6) mixture [8]. Isotropy of the IPyC layer, which influences irradiation performance, is determined by the gas mixture concentrations, deposition temperature and coating rate [6]. Proper coating will result in layers with density around 1.9 g/cm^3.

1.2.1.4 Silicon carbide. The third coating layer TRISO fuel has is SiC. This relatively dense layer is used to contain both gaseous and metallic fission products and also withstand internal pressure caused by fission product buildup and CO formation [1,6]. As such, the SiC acts as a pressure vessel for the fuel particle.

SiC is so commonly used as a TRISO coating because it exhibits high temperature strength, stability in radiation environments, and low activation properties [10]. Mechanically, SiC is useful because it possesses among the highest hardness values of covalent materials [11]. Furthermore, its strength properties are unaffected by surface or internal flaws [10]. SiC begins to thermally decompose near 2000 degrees Celsius, a safe step above the predicted accident scenario fuel temperatures in the range of 1600 to 1800 degrees Celsius [5].

Chemical deposition of the SiC layer requires hydrogen and methyl tri-chlorosilane (CH_3SiCl_3) [5,8]. Similar to the other coating layers, the coating parameters determine the isotropy and microstructure of the layer. Ideal microstructure requires coating rates slower than one micron per minute in the temperature range of 1500 to 1650 degrees Celsius [6,12]. At this temperature range, stoichiometric cubic SiC is produced, which exhibits improved radiation tolerance compared to anisotropic variations [13].

1.2.1.5 Outer pyrocarbon. The outermost layer of TRISO fuel is the outer pyrocarbon (OPyC) layer. The OPyC and IPyC layers have the same structure. This layer serves as support for the SiC layer, provides an additional fission barrier, and provides a bonding surface for the fuel pellets when they are embedded into compacts or pebbles [1,6].

There are two distinct HTGR designs that utilize TRISO fuel: pebble bed and fixed core. The program in Germany is highly focused on the pebble bed design in which TRISO particles are pressed into 60 mm diameter pebbles using graphite powder and an organic binder [5,6]. These pebbles serve as the base fuel element for the reactor. The benefit of this design is that the fuel is able to cycle through the reactor during operation which eliminates the need to shut down to refuel. This luxury comes at the expense of a core configuration that is more difficult to analyze because of how it changes over time. In the United States, fixed core designs were used which used TRISO particles by pressing them together with petroleum pitch, graphite shim and graphite flour into the

form of cylindrical fuel compacts. The fixed core Japanese HTTR utilizes cylindrical tube compacts which are 39 mm tall with an outer diameter of 26 mm and an inside diameter of 8 mm [6]. These compacts are arranged into fuel rods in an assembly closely resembling the fuel rods in PWRs and BWRs.

All of the TRISO layers functionally complement each other. As a whole, the particle allows for high burnup while operating at high temperatures and containing fission products.

1.2.2. Irradiation and Temperature Effects. Despite the tolerance SiC and PyC have under irradiation that made them the materials of choice for use in TRISO fuel, flaws in the coating layers can lead to failures under the high flux and temperature in a HTGR. Effects that detrimentally effect TRISO fuel coating layers include fission product buildup, irradiation-induced dimensional change (IIDC), temperature gradients and irradiation creep. These effects lead to the loss of mechanical and thermal properties and sometimes catastrophic failure of the particle [5,10,13,14].

The fission process inevitably yields a large amount of fission products that must be dealt with. Burnup, fluence, temperature, temperature gradient, material stress, and fuel properties all influence the quantity of fission gas production. These fission products pose a threat to fuel integrity because they can lead to swelling and stress buildup in the particle. When a sufficient amount of fission product gases have been formed, they nucleate into bubbles. Xenon and krypton are of particular concern because they are common fission products and have several stable isotopes, leading to substantial accumulation over time [5,14,15].

When TRISO coating layers are irradiated, IIDC is another effect which leads to an increase in particle size. The swelling is due to void formation rather than the nucleation of bubbles as caused by fission product buildup. IIDC initiates from the direct interaction of neutrons with a material. Because the fuel coating layers are in direct contact with the fuel, they are subject to high neutron fluence relative to other reactor components. When a high energy neutron knocks an atom out of its lattice position, a cascading effect begins and many additional displacements occur [15]. These displacements create vacancy and interstitial pairs in the material. These pairs are one dimensional point defects that on their own do not play a significant role in altering

material properties because a majority of them recombine, especially at temperatures as high as those experienced by TRISO fuel during operation. Interstitials and vacancies that do not recombine, however, can form into larger two or three dimensional imperfections [15]. The three dimensional case is known as a void. Accumulation of numerous voids leads to swelling of the material.

Cracking of the coating layers and debonding of the PyC-SiC interface are the primary issues caused by IIDC [5,14]. Initial exposure to neutrons triggers shrinkage in PyC; experiments by Petti et al. with peak fluences near $2x10^{25}$ n/m^2 showed that under irradiation the PyC layer shrinks tangentially while swelling in the radial direction [5]. This can lead to sufficient tangential stresses for cracking to occur.

Creep is a common problem among materials, especially in high temperature environments [15]. Creep leads to permanent deformation in materials undergoing constant stress below their yield point. Irradiating the material enhances the rate and severity of creep [15]. Creep effects within the coating layers lead to a permanent increase in the stress and strain of the particle [14]. Another temperature effect that can affect TRISO fuel is kernel migration. This effect is limited to particles with excess CO formation and is caused by a temperature gradient over a TRISO particle. The gradient leads to CO migrating to the cold side of the particle, where CO molecules interact to form CO_2 and solid carbon [14]. As carbon builds up, the kernel is pushed away from the center of the particle toward the hot side of the particle.

The quality control of TRISO fuel is vital in combating the cumulative temperature and irradiation effects the fuel must endure. Fission gas pressure, IIDC, and irradiation creep all exert a tension force on the TRISO particle which can lead to failure by cracking as seen in Figure 1.1.

Implementing productive quality control methods is a vital step toward ensuring the fuel being used in reactors is of the highest quality. Reducing the quantity of flawed fuel in a reactor leads to minimization of fission product release and ultimately, increased reactor efficiency.

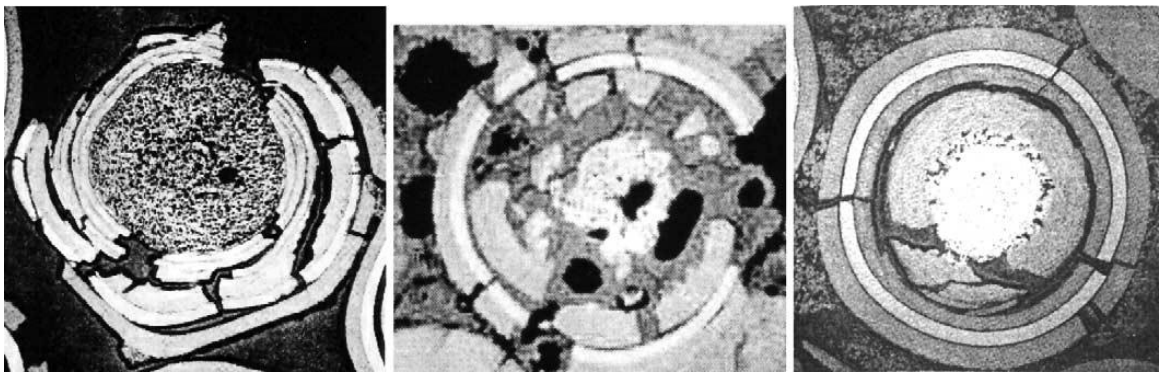

Figure 1.1. Failure of the coating layers and kernels of (from left to right) a fertile fuel particle, UO_2 particle and UC_2 particle [5]. In each case, failure of all coating layers occurred due to temperature and irradiation effects.

1.2.3. Importance of Determining Density. The manufacturing process for TRISO fuel relies on many procedures that could potentially lead to defects. Defects vary from missing coating layers to anisotropic microstructure to incorrect coating layer density. General Atomics used decades of TRISO fuel production expertise to assemble a list of the most important defects to detect in TRISO fuel, shown in Table 1.1 [4].

Table 1.1. The most important TRISO fuel manufacturing defects as determined by General Atomics [4].

Defect
Missing buffer coating
Heavy metal contamination
Defective SiC
Spatial defects penetrating the SiC layer
Incorrect grain size and structure
Free silicon or free carbon
Structural flaws
Impurities
Incorrect IPyC density
Incorrect IPyC thickness
IPyC anisotropy
OPyC anisotropy

In addition to the defects listed in Table 1.1, IAEA created a list of criteria used to qualify the German fuel program, in which thickness of coating layers, density of coating layers, and SiC layer defects were listed [3]. These lists illustrate that both the international and United States communities realize the importance of measuring TRISO fuel density as a quality control measure. Proper functionality of each of the coating structures can be inferred from the density. For the buffer layer, the density must be sufficiently low to indicate adequate void space for fission product detainment. The IPyC layer must be dense enough to prevent chlorine from reacting with the fuel during the SiC deposition process. The maximum theoretical density is sought for the SiC layer, as porosity would decrease the particle strength and irradiation tolerance [12]. Finally, the OPyC layer must be dense enough to strengthen its function as the final fission product barrier as well as adequately protect the SiC layer when the TRISO particles are formed into fuel compacts or pebbles.

Because of the rigorous manufacturing and performance standards placed on TRISO fuel it is inheriting an ever increasing amount of responsibility for fission product containment [1]. To ensure that fuel performs as expected under HTGR operating conditions, the material properties of the manufactured fuel, such as density, must consistently exhibit high accuracy. Density is a particularly useful property to measure because it is linked to the structural and irradiation performance of the fuel. Additionally, other properties such as porosity and mass can be inferred from density and it can be measured nondestructively.

In the nuclear power industry, public support has played a strong role in determining the success of nuclear projects. In 1953, after Eisenhower's Atoms for Peace speech, nuclear power had a strong reputation. In turn, this was tarnished by the Three Mile Island and Chernobyl accidents, which effectively ended many ongoing nuclear projects in the United States and Europe. Safe nuclear operation over the past 30 years coupled with public concern for carbon dioxide emissions has reinvigorated support for the nuclear industry [16].

Despite increased support of nuclear power, public concerns still exist, the largest of which are spent fuel storage and proliferation. These concerns are balanced by a need to control greenhouse gas emissions, depletion of natural gas resources, energy security,

energy prices, employment, and economic development [16]. The strong public participation in the United States necessitates public approval for commercial deployment of HTGRs. As such, the manner in which the technology is presented to the public has a drastic impact on its future success.

Even with public support of nuclear power, the HTGR will have difficulty establishing itself as a new type of reactor if not introduced correctly because it relies on a new set of safety principles and there is limited industry experience in operating the reactors [16]. Boasting the safety features of the HTGR also runs the risk of undermining public opinion of traditional reactor designs.

Hannink et al. presents a list of HTGR characteristics that convincingly address the most prominent public concerns about nuclear power [16]:

- TRISO coatings contain radionuclides during operation and in long-term storage.
- Improved burnup of fuel reduces spent fuel waste and combats proliferation.
- Core transient behavior is inherently slow.
- Core decay heat is removed passively.
- Even with loss of coolant pressure, no AC powered equipment and no timely operator action, a core melt could not occur.
- Improved safety margins allow the reactor to deliver steam and heat to nearby industry.
- A smaller plant size reduces upfront costs and lends itself to incremental expansion.

Introducing such unadulterated facts to the public maximizes the potential for strong public support.

In addition to density information, radiographs contain information on other manufacturing defects, such as missing coating layers, defective coating layers, and cracks. This diversity of information can collapse several previously required quality control measures into one.

By having a greater number of practical quality control measurements imparted on TRISO fuel, more confidence can be vested in the fuel being put into reactors and more feedback can be given to improve the manufacturing process. Determining the

density of TRISO fuel is one aspect of quality control that supports the efficient and safe operation of HTGRs.

1.2.4. Current Methods of Inspecting TRISO Fuel. Presently, several methods of determining the density of TRISO fuel are implemented. Since HTGR reactors are not utilized commercially, a large scale density measurement technique has not been required. Part of demonstrating the HTGR as a viable commercial reactor will be verification of a quality control method that can handle large scale fuel production. Most of the quality control methods used today are incapable of fast inspection and are based on 1970s and 1980s technology [4].

The sink-float method of determining density utilizes a column filled with two liquids, one that is denser than the object and one that is less dense. The density of the object is determined by its buoyancy in the mixture relative to reference objects. This method suffers from long preparation time, inability to be automated, and inability to measure density of individual layers nondestructively.

Computed tomography involves taking a large number of radiographs at different object orientations. This method can provide detailed information on the attenuation of the object but comes at the price of slow data acquisition rates. Typical data sets contain around 180 or 360 images in addition to others to correct for detector response and noise. Imaging time for a single object can be on the order of hours and contain gigabytes of data.

Ceramography is analysis of ceramic microstructures. It is a destructive technique that involves cutting and polishing the particle to be examined. Measurements can be made of the particle grain properties as well as its porosity [17]. Density information can be extracted from the porosity information. This process is not practical for large scale fuel production because it is both time consuming and destructive.

Pacific Northwest National Laboratory began an investigation in 2003 investigating methods of online quality control. Among the methods tested are electromagnetic, resonance ultrasound spectroscopy, optical surface inspection, acoustic microscopy, transmission and diffuse field ultrasound, x-ray radiography, and computed tomography [4]. Several of these techniques excelled in terms of inspection rate although

most were unproductive in measuring useful quality control parameters. Density was not measured by any of their techniques.

The density measurement methods in use today simply do not have the ability to function as quality control methods for commercial production of TRISO fuel in terms of time or economics. As a step toward this goal, an alternative method which is non-destructive, quick, robust, and potentially automated has been developed by utilizing typical x-ray radiography.

1.3. X-RAY RADIOGRAPHY

An x-ray radiography system consists of a source of x-rays, an object or objects to be imaged and a detector. The system components of relevance to this paper are discussed in this section. An x-ray source has two main components, the generator and the x-ray tube. An x-ray generator is responsible for providing the x-ray tube with a consistent source of voltage and current. The generator used in this paper constantly measures both of these parameters to ensure a stable x-ray output [18]. The generator is connected to the x-ray tube, which contains a diode whose cathode is heated to very high temperatures, around 2200 degrees Celsius, to thermionically emit electrons [19]. Since voltage is applied between the cathode and anode, the freed electrons are accelerated toward the anode which is often made of tungsten. Tungsten is commonly used because of its 3380 degree Celsius melting temperature and high density [19]. Some of the accelerated electrons interact with the anode atoms to generate Bremsstrahlung radiation, which is the energy slowing electrons lose after being deflected by a target nuclei. Bremsstrahlung radiation is the largest contributor of photons in standard x-ray radiography [19]. X-rays generated via the Bremsstrahlung process exhibit an energy distribution that is dependent on the energy loss of the source electron. If the source electrons have more energy, more energy can be converted in the Bremsstrahlung process; the maximum x-ray energy is therefore limited by the potential applied in the x-ray tube diode because it governs the energy of the electrons.

The constant x-ray beam being generated by the x-ray tube undergoes interaction with the imaged objects. As an x-ray in the energy range being considered, less than 50

KeV, passes through a medium it can interact with atomic electrons via photoelectric absorption or one of two scattering reactions. Photoelectric absorption is an interaction between an x-ray and an atomic electron where the photon is absorbed by the electron and converted into kinetic energy, ejecting the electron from its parent atom. Incoherent (Compton) scattering also results from the interaction between an x-ray and electron but the photon is deflected instead of absorbed. In this process, the x-ray loses a certain amount of energy depending on the severity of the deflection angle [18]. The final photon interaction in this energy range is coherent (Rayleigh) scattering. Coherent scattering involves the interaction of a photon with all of the electrons in an atom [19,20]. The resulting photon has lost little energy and has changed slightly in direction. Of the three interactions, coherent scattering is the least likely to occur. Since all of these interactions are between the x-ray and atomic electrons, they are competing processes; if an absorption reaction occurs, it eliminates the chance for a scattering event to occur. Because they have more electrons, atoms with higher atomic number more favorably undergo photon interactions and thereby attenuate more photons. The resulting difference in photon intensities among differing materials is what is utilized to form images once the photons are detected.

Detectors for x-rays are commonly two-dimensional arrays of pixels consisting of a scintillating material, photodiodes, and signal processing components. The detector used in this paper uses a gadolinium oxysulfide scintillator with a terbium impurity (Gd_2O_2S[Tb]); when an x-ray strikes the scintillator, it is converted to visible light which is in turn detected by a silicon photodiode. Through this indirect detection method, an electrical signal proportional to the energy of incident radiation is generated for each detector pixel [21,22]. Mapping all of the pixels together forms an x-ray image.

2. METHODS

This section contains the background discussing the feasibility of the thesis objective, the assumptions that must be made to utilize the proposed algorithm, and a description of the simulated and experimental methods used to achieve the objective.

2.1. THEORETICAL BACKGROUND

2.1.1. Equations and Principles. Utilizing x-ray radiography, a new method for determining the density of TRISO fuel coating layers has been developed. The method utilizes an inherent property of x-ray radiographs: the brightness of a pixel (*P*) in a radiograph is proportional to the energy of the radiation absorbed by that pixel (*I*). This is illustrated by Equation 1.

$$P = cI \tag{1}$$

This property of radiography is fundamental to all x-ray imaging applications from radiology to nondestructive testing. As a collection of photons traverse through a medium a portion of them will interact with atomic electrons and not make it to the detector. Equation 1 describes how the brightness of detector pixels in an image will be different for pixels obscured by an object and those which are not.

Attenuation will vary depending on the characteristics of the medium or media being imaged. These characteristics are related to the intensity (energy) of the absorbed radiation by the Beer-Lambert Law, shown in Equation 2. The Beer-Lambert Law characterizes the intensity of uncollided photons after traversing through a medium.

$$I = I_0 exp\left[\left(\frac{\mu}{\rho}\right)\rho t\right] \tag{2}$$

The equation shows the dependence of the final intensity on the initial intensity (I_0) of the x-rays and three characteristics of the attenuating medium, the attenuation coefficient (μ/ρ), density (ρ), and thickness (t). The exponential nature of attenuation is also evident

from the equation. The general form of the Beer-Lambert Law in Equation 2 can be expanded to include multiple attenuating media over the entire photon energy range, as seen in Equation 3.

$$I = \int_0^{\mathrm{E_{max}}} I_0(E) exp\left[-\sum_{j=1}^{5}\left(\frac{\mu(E)}{\rho}\right)_j \rho_j t_j\right] d\mathrm{E} \quad (3)$$

In this form, the polychromatic nature many x-ray sources exhibit is accounted for. Both the initial number of photons and the mass attenuation coefficient of each material are functions of energy. A sample x-ray spectrum generated by an x-ray tube with a tungsten target is shown in Figure 2.1.

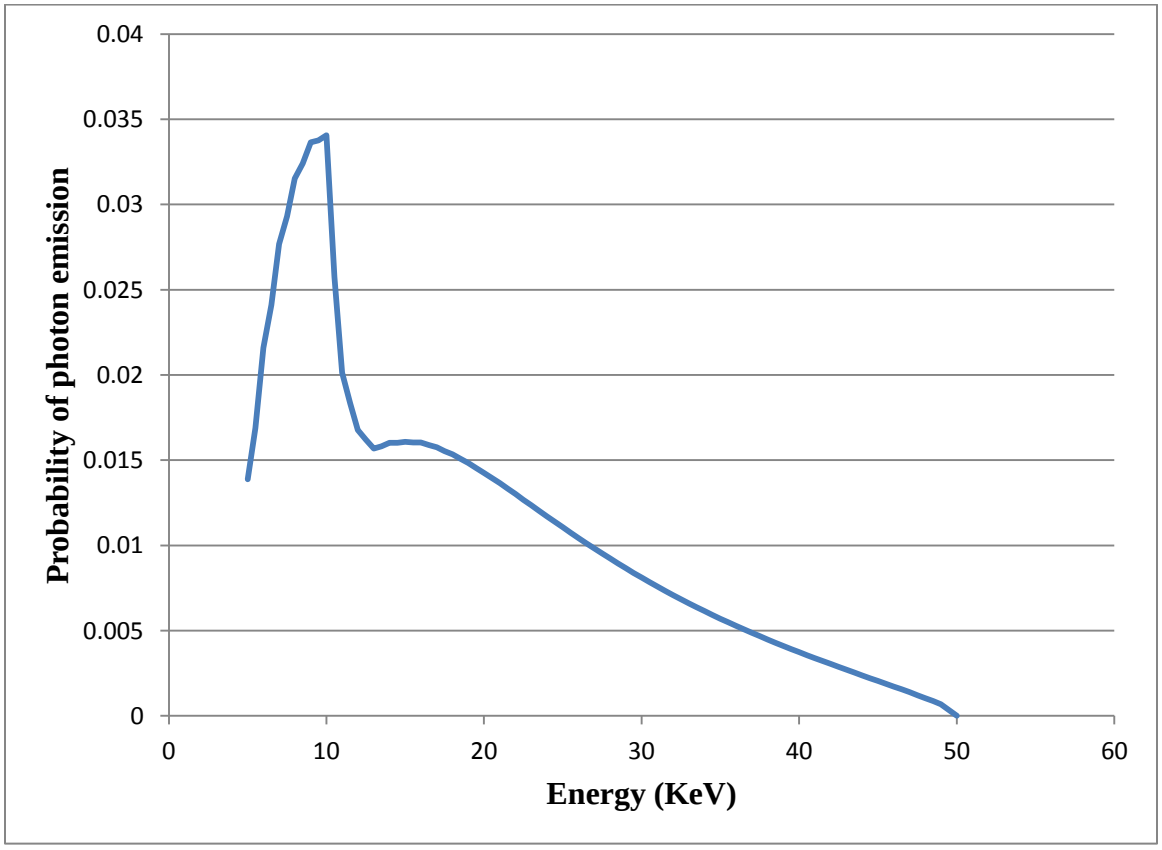

Figure 2.1. A photon energy distribution created by an x-ray tube set to 50 KVp.

The curve in Figure 2.1 represents the values of $I_0(E)$ in Equation 3 for a 50 KVp setting. The complex shape of the photon energy distribution eliminates the option of directly calculating the integral in Equation 3. Instead, the integral in is approximated by the summation in Equation 4.

$$I = \sum_{i=1}^{n} I_{0,n} exp\left[-\sum_{j=1}^{5}\left(\frac{\mu}{\rho}\right)_{i,j}\rho_j t_j\right] \quad (4)$$

In this form, discrete, sampled data can be used for the x-ray energy distribution and mass attenuation coefficients to analytically determine density. The accuracy of the density calculation depends on the quality of the input data and the severity of the approximations associated with using Equation 4.

2.1.2. Assumptions and Justifications. Utilizing the Beer-Lambert Law for density calculation requires several assumptions to be made. This section describes all of the assumptions used in the density calculation algorithm and provides justifications for their validity.

The most apparent assumption that is inherent to the Beer-Lambert Law is neglecting the contribution that scattering radiation has on the image. It assumes that if a photon interacts with the material it is removed from the system and will not reach the detector. In the energy range being considered, below 50 KeV, photon interactions consist entirely of photoelectric absorptions, incoherent scatterings, and coherent scatterings. All of the possible photon-material interactions resulting from scattering and absorption are depicted in Figure 2.2. The assumption holds well for radiation that passes through the object without interaction, is absorbed via photoelectric absorption, or is scattered at an angle away from the detector, as illustrated in Figure 2.2 A, B, and C, respectively.

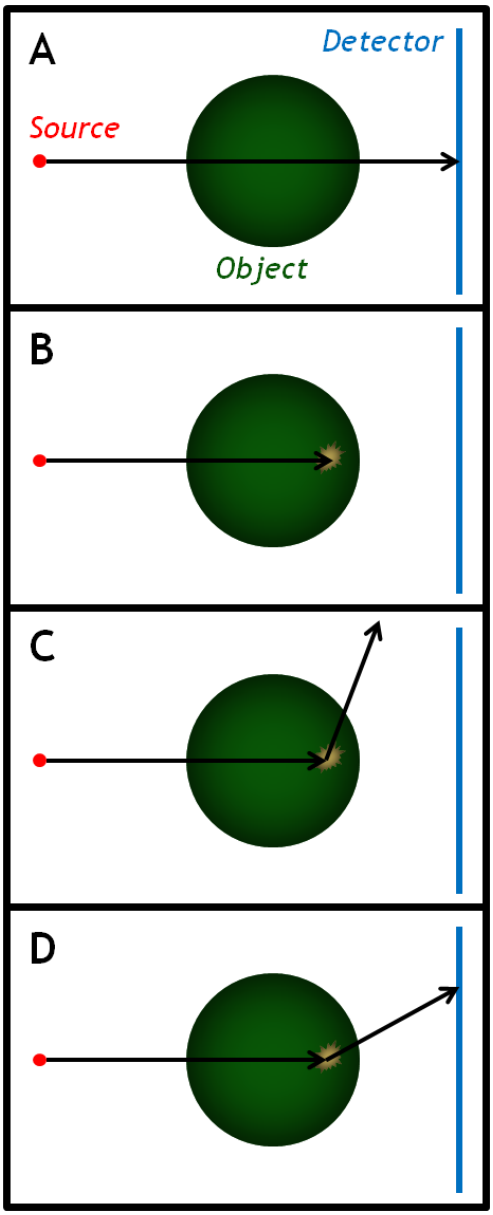

Figure 2.2. Possible photon-material interactions below 50 KeV. ***A*** represents no interaction, ***B*** represents photoelectric absorption, ***C*** is a scattering collision that does not contribute to the image, ***D*** is a scattering collision that contributes to the image.

The only situation where the assumption proves invalid is represented in Figure 2.2 D in which both a scattering reaction occurs and the scattered photon strikes the detector. To evaluate the efficacy of the assumption, the relative numbers of uncollided and absorbed photons were compared to the number of scattered photons after

transmission through an object representing TRISO fuel using the Beer-Lambert Law from Equation 4. Three locations with differing material path lengths were chosen for this evaluation. They are shown in Figure 2.3.

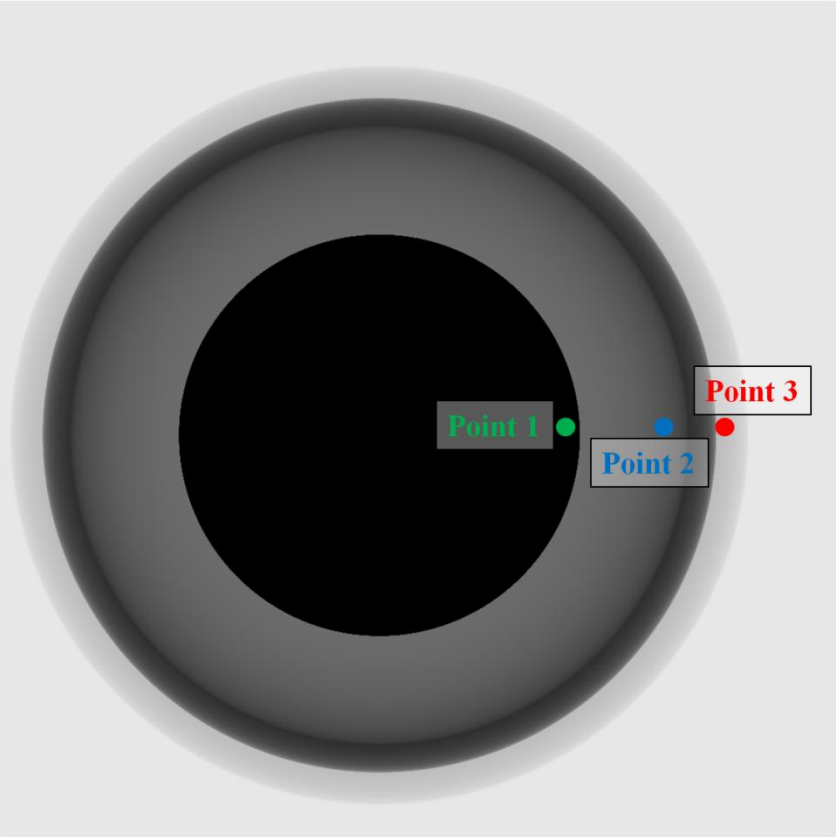

Figure 2.3. Locations at which scattering and absorption interactions in TRISO fuel were compared. The three locations represent the full range of path lengths and materials a photon could interact with.

Multiple points were selected because different locations in the fuel have different path lengths that an x-ray will traverse. Because the points in Figure 2.3 represent dissimilar path lengths of different material combinations, they will fully characterize the scattering and absorption interactions for the entire particle. The result of this comparison for all three locations is shown in Table 2.1.

Table 2.1. Comparison of scattered photon to non-scattered photons from a 30 KVp photon distribution in a TRISO particle. The results in this graph are extremely conservative as they do not illustrate the competitive nature of photon-electron interactions.

Layer	Density (g/cm^3)	Path length at point 1 (μm)	Path length at point 2 (μm)	Path length at point 3 (μm)
Kernel	10.97	141.3	0	0
Buffer	1.10	354.5	0	0
IPyC	1.90	106.3	269.4	0
SiC	3.18	87.2	160.7	0
OPyC	1.90	95.1	140.3	316.7
Percentage of photons that interact via absorption		99.99%	64.23%	19.57%
Percentage of photons that interact via scattering		52.33%	5.35%	1.83%
Ratio of absorption photons to scattered photons		**1.91**	**12.01**	**10.67**
Ratio of non-scattered photons to scattered photons		**0.91**	**17.70**	**53.51**

The calculations were performed using a 30 KVp photon distribution because it represents the higher end of settings used in radiographs of TRISO fuel. Lower KVp settings would lead to a larger ratio of absorption to scattering reactions so the results shown are conservative for such settings. Three different quantities are used as points of comparison in Table 2.1. First, the percentages of photons that interact via absorption and scattering are compared. If only absorption or scattering events occurred in the TRISO fuel, these quantities represent the percentage of photons that would undergo an interaction. For all three of the path lengths examined, it is clear that the absorption interaction is dominant. In fact, the absorption attenuation coefficient is so large for the kernel that nearly all the photons passing through it will be absorbed.

The next comparison shown in Table 2.1 is the ratio of these two results. This ratio represents how many times more likely it is for an absorption reaction to occur than a scattering reaction. For the kernel, this value is rather low but is counteracted by the

fact that nearly all of the photons in this region will be absorbed and not make it to the detector. For the photons that do not traverse through the kernel, the number of absorption interactions is an order of magnitude higher than the scattering interactions.

The third comparison compares the number of non-scattered photons to the number of scattered photons if scattering reactions were the only interactions that took place. Equivalently, this compares the number of photons which have no chance of creating a false reading on the detector to those that could potentially create a false reading. As with the previous comparison, the result in the kernel is overshadowed by the complete attenuation of photons in that region. The photons that do not traverse the kernel have a significantly higher chance of contributing positively to the image than degrading it.

All of the results in Table 2.1 are for a simple test that does not represent a true physical quantity because in reality scattering and absorption interactions are competing processes that cannot be separated. This also makes the results in Table 2.1 extremely conservative. The results in the final row assume that no absorption reactions are occurring when in reality, absorption is occurring and removing a large majority of photons from the system. Additionally, the calculations do not reflect that even if a scattering interaction occurs, it doesn't mean it will make it to the detector. Generally speaking, regardless of which materials the photons traverse, the probability of a scattering reaction contributing negatively to the image is insignificant. This can be attributed to a low scattering cross section relative to absorption cross section for the TRISO materials as well as the small size of the TRISO particle relative to the scattering mean free path of the TRISO materials. The scattering and absorption attenuation coefficients for the materials used are plotted in Appendix A [23].

A second assumption inherited by using the Beer-Lambert Law is that within each TRISO layer, the composition is homogeneous and without impurities. Algebraically, this means that the attenuation coefficients and densities of the coating layers are not functions of position through the coating layer. Fortunately, manufacturers strive for isotropic, pure, and even coating layers to maximize physical and irradiation strength of the particles [12]. Methods of removing impurities such as sintering are integrated into the particle construction to achieve these goals. During the chemical vapor deposition

process, inert argon or hydrogen gas is used in combination with strictly controlled coating gas. Because of the inherent precautions taken by fuel manufacturers and the need for particles to be isotropic to make the commercial deployment of HTGRs possible, credibility is given to this assumption.

Finally, in calculating the x-ray path lengths from the source to detector pixels it is assumed that the source is a point. The experiments conducted in this paper utilized an x-ray tube with a circular focal spot 0.4 mm in diameter. The finite size of a focal spot dictates the measureable feature size in an x-ray radiograph. As the distance between the source and detector is increased, the negative effects of a large focal spot size are reduced. The experiments in this paper utilized a source to detector distance 1100 times greater than the focal spot size so the error in calculating path length due to this effect will be on the order of 10^{-7}.

2.2. ALGORITHM

With a valid concept in place, an algorithm was developed. Robustness of the algorithm was a key design goal. Just by inputting an image and describing the imaging setup, the algorithm can extract density of each coating layer. Equation 4 is used as the basis for the calculation; as such, each term in Equation 4 was determined as accurately as possible so density could be determined precisely. More specifically, the energy spectrum of the x-ray tube, attenuation coefficients of each material, and material path length data were determined.

2.2.1. Energy Spectrum Determination. Characterization of energy spectra is a predictable yet complex process. A spectrum depends on the x-ray tube voltage potential, x-ray tube anode composition and geometry, and filter materials. Spectra can be measured experimentally with an energy resolving detector or generated using computer code such as Monte Carlo N-Particle (MCNP) transport code. Experimental measurements, however, suffer from detector energy biases and attenuation effects when testing outside of a vacuum. For this paper, a deterministic x-ray spectrum generator called SpekCalc was used [24]. Spectra generated by SpekCalc closely follow those generated by MCNP type code.

2.2.2. Attenuation Coefficient Determination. Each element has distinct attenuation characteristics related to its atomic number and the energy of the interacting photon. Molecules and mixtures of elements exhibit a combination of the attenuation characteristics of their constituent atoms. Many experiments have been performed to determine the attenuation coefficients of materials. As part of the algorithm, experimentally determined attenuation coefficients by the National Institute of Standards and Technology were used [23]. As an example, the mass attenuation coefficient of silicon carbide is shown below in Figure 2.4.

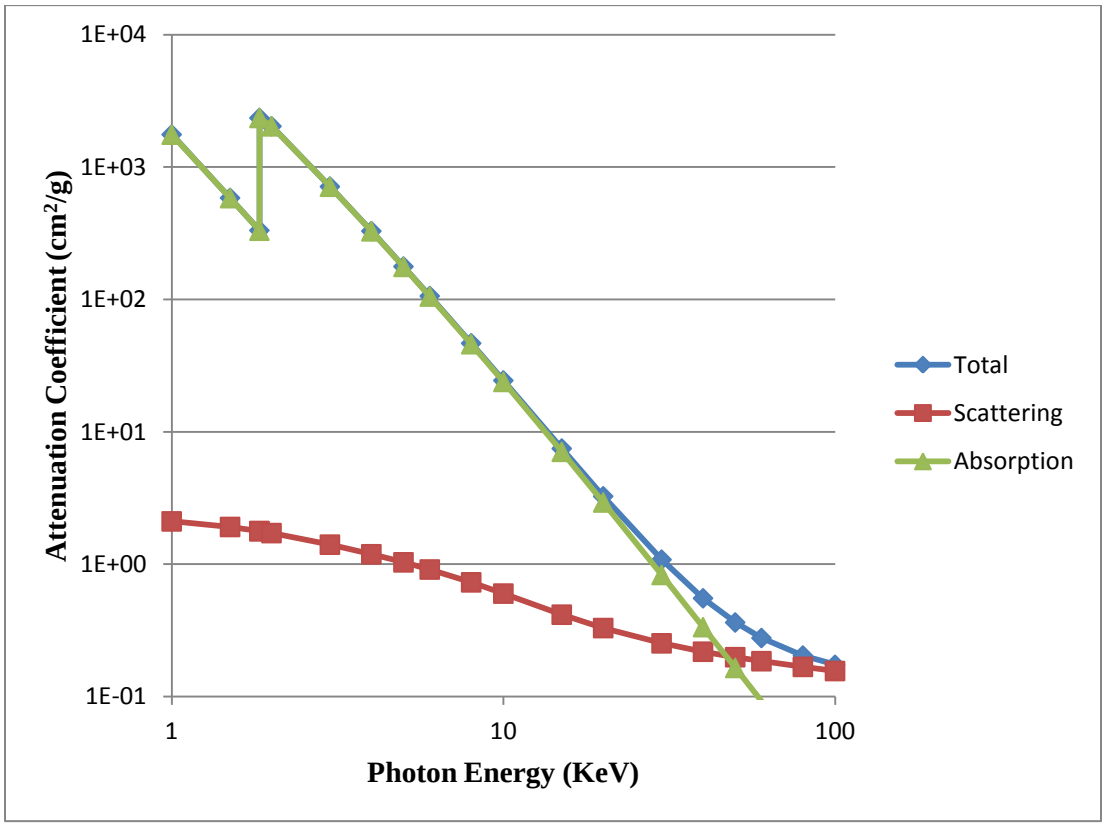

Figure 2.4. Mass attenuation coefficient of silicon carbide for 0 to 100 KeV photons. For lower energies, photoelectric absorption is the dominant interaction.

The contributions from photoelectric absorption are shown separate from and combined with the contributions from incoherent and coherent scattering. The figure shows the power law dependence attenuation coefficient has with energy and the dominance of the absorption attenuation coefficient for photons of 50 KeV and lower energies. The discontinuity in the graph is known as a k-edge and coincides with the binding energy of the electrons in the innermost electron shell, the k-shell. This discontinuity is created because of photoelectric absorption which can only occur when the energy of the incident photon is greater than the binding energy of the electron. As Figure 2.4 depicts, for photons with energy slightly greater than the binding energy, more electrons are available for photoelectric absorption and the attenuation coefficient is larger than photons with slightly less energy than the binding energy.

2.2.3. Path Length Determination. Photon path length varies from pixel to pixel because of the non-uniform thickness of the object and cone beam geometry of the x-ray source. For a comprehensive view of an imaged object, the photon path length for every material at every pixel is required. The process in Figure 2.5 shows how path length is calculated.

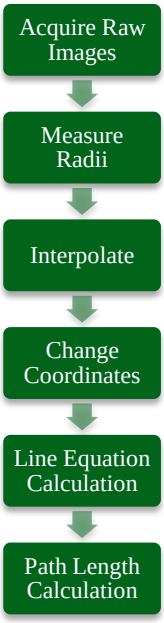

Figure 2.5. Process used for determining path length from a radiograph.

To start, raw images are acquired at one to eight projection angles, forming a miniature tomography set. Proper imaging practice should be exercised in selecting the potential, exposure time, and geometric setup to ensure optimal contrast between the coating layers. Once proper images are obtained, kernel and coating layer radii can be measured.

Since TRISO fuel is roughly spherical in shape, it is convenient to describe the radii of each layer with respect to angle. To do this, the TRISO fuel image is remapped to polar coordinates based on the center point of the fuel kernel. While the coating layers in TRISO fuel often have imperfections in their sphericity, the kernels are much closer to ideal. Coincidentally, the kernel of TRISO fuel is the darkest spot on the image. To find the center, the image is thresholded so that only the kernel is visible and then the maximum width and height of the kernel are determined by checking the number of pixels in each row and column of the thresholded image, respectively. This process applied to the rows of a fuel image is illustrated in Figure 2.6.

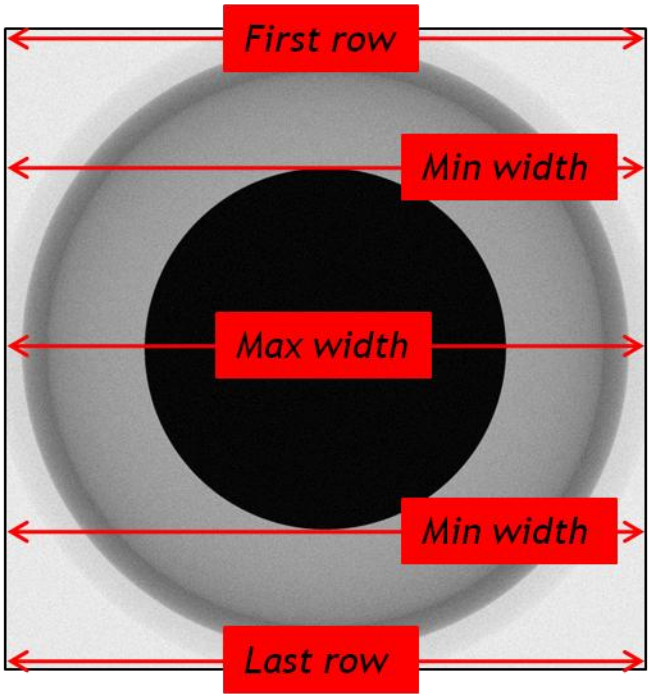

Figure 2.6. Width of a TRISO fuel kernel with respect to image row; used to calculate the centroid. This operation is performed after thresholding the image.

Starting at the top of the image in Figure 2.6, the algorithm reports zero pixels corresponding to the kernel. As the image continues to works its way through the rows, it keeps reporting zero kernel pixels until it reaches the top of the kernel and it records a non-zero number of black pixels in the row. Working its way further through the image, this number becomes larger until the max width is reached and then the value begins to descend back toward zero. The row containing the maximum value is registered as the centroid row. Repeating this process over the columns of the image provides the centroid column. With the centroid location of the fuel determined, the image is remapped, which involves specifying coordinates in (r, θ) and determining their value via bilinear interpolation from (x, y) coordinates in the original image. Figure 2.7 shows the result of this process.

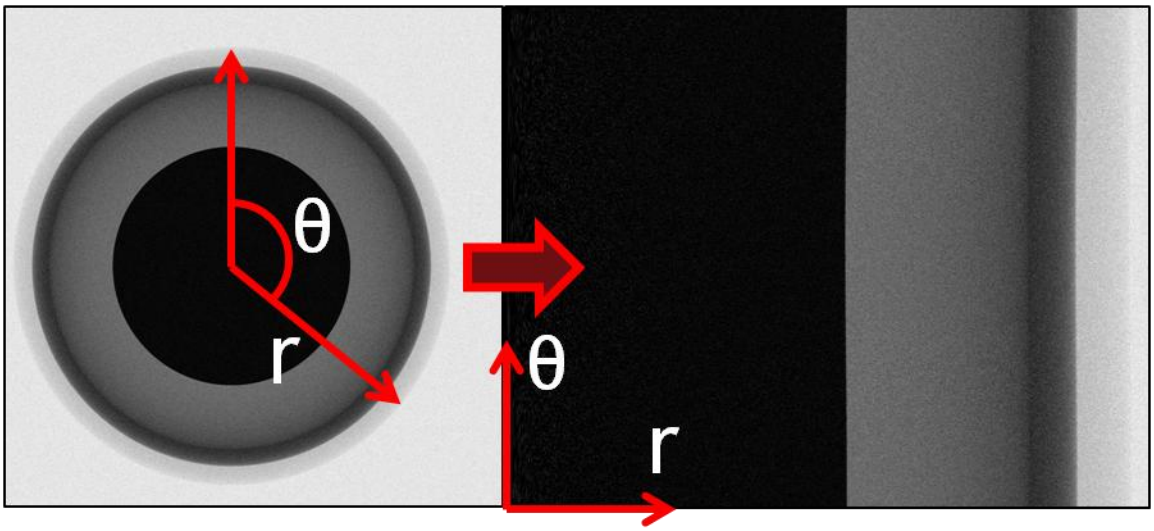

Figure 2.7. Remapping rectangular coordinates to polar coordinates to measure the radii of TRISO layers.

In this transformed form, the radii can be conveniently measured with respect to angle around the TRISO fuel. This measurement process is repeated for every image in the set.

Since the radii measured in the radiographs were obtained from a finite number of images, interpolation is used to define the complete shape of the object. Interpolation is performed over two angles: the inclination angle (θ) which is the angle from the top of a TRISO image to the center of the kernel to another point on the layer being measured, as depicted in Figure 2.7, and the azimuth angle (ϕ) which is the angle the radiograph projection was taken at. These angles are graphically displayed in Figure 2.8. The figure shows how the data from an image set containing four radiographs would be compiled before interpolation. Additionally, the definitions of inclination angle and azimuth angle are depicted on a TRISO particle.

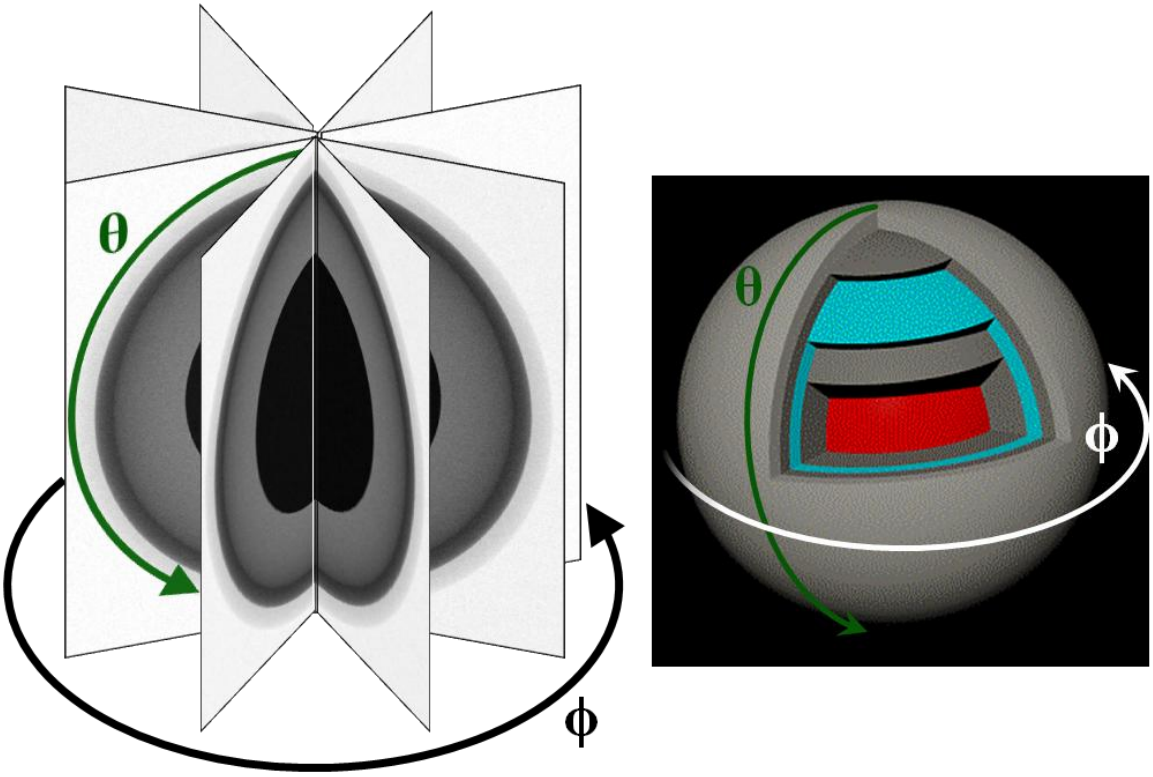

Figure 2.8. Definition of the inclination angle (θ) and azimuth angle (ϕ). The angles are shown in relation to individual radiographs (left) as well as a TRISO fuel particle (right).

The roughly spherical shape of the fuel creates a situation in which fewer radiographs are required to accurately define the shape compared to a more complex geometry. The angle spacing required for interpolation is defined by the magnification due to the imaging geometry. Figure 2.9 shows the relationship between interpolation angle and pixel size. The pixel size is enlarged in the figure to demonstrate the concept.

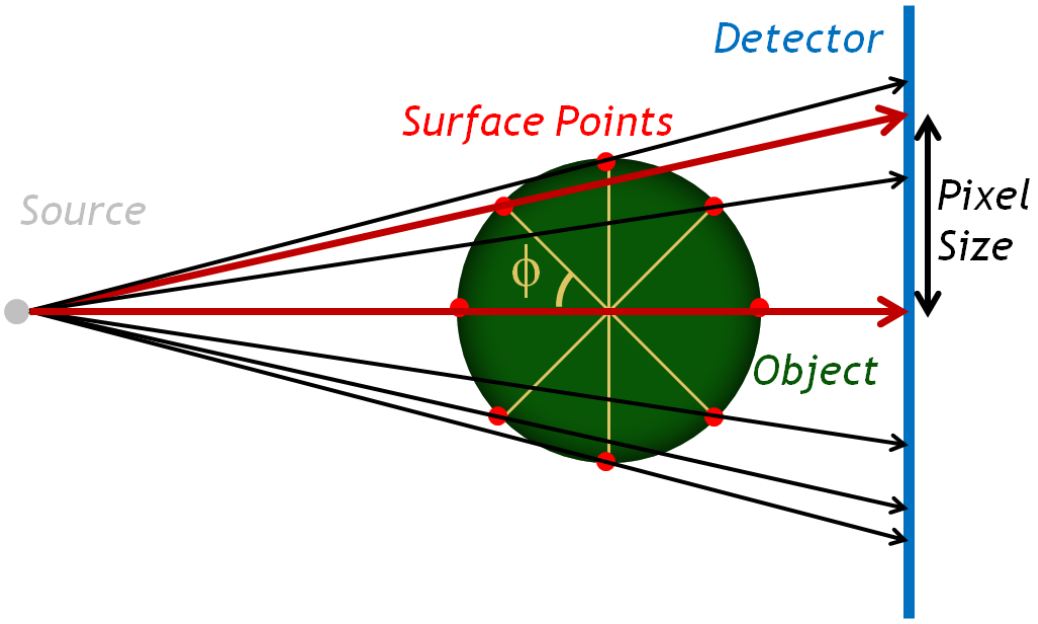

Figure 2.9. A simplified diagram showing the relationship between the pixel size and the required interpolation angle for adequate sampling. If the interpolation angle (ϕ) becomes too large, then there will be insufficient data to map thickness data to every pixel. The image is not to scale; the pixel size is enlarged significantly to demonstrate the relationship.

As Figure 2.9 shows, the interpolation angle between points is magnified by the imaging setup geometry. The two red path lengths are those that form the largest gap between two sampled points. The spacing of surface points in the figure shows the minimum sampling rate needed to form an image. If the spacing between the two points was any larger, the projection of the points on the detector would be spaced farther apart

than the pixel size causing some pixels to miss data. An image that is magnified more will be projected onto a greater number of detector pixels and therefore requires finer interpolation to draw from.

Once the data is interpolated with respect to the inclination and azimuth angles, the data is in the form of (r, θ, ϕ) coordinates. These coordinates are converted to Cartesian coordinates to conform to the geometry of the imaging setup shown in Figure 2.10. The origin of the coordinate system was chosen so the x and y-coordinates are zero at the negative most part of the detector surface and the z-coordinate is zero when in line with the source. This convention is standard for imaging applications and eliminates negative values.

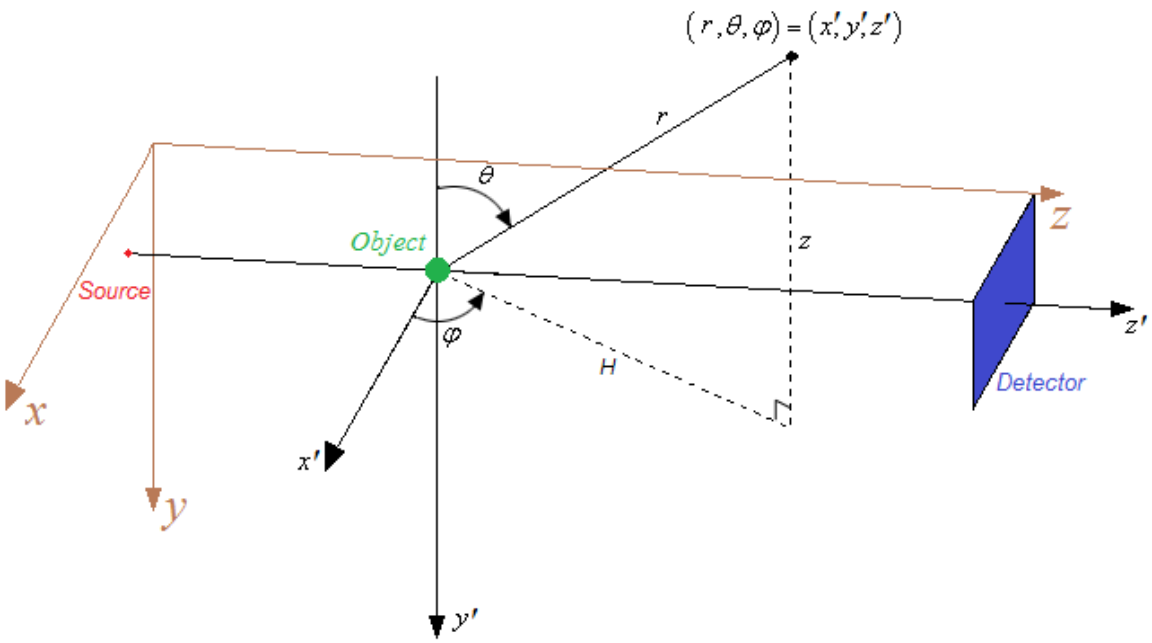

Figure 2.10. The coordinate system used.

With a fully defined geometry, the radiation paths through the object are determined. Since the fuel is not perfectly spherical, algebraic equations cannot be used to define its layer surfaces. Instead, a robust method was developed to determine the

location of intersection between photons and an imaged object. The method works for any geometry in which uncollided radiation has a single entry and exit point for the object, illustrated in Figure 2.11.

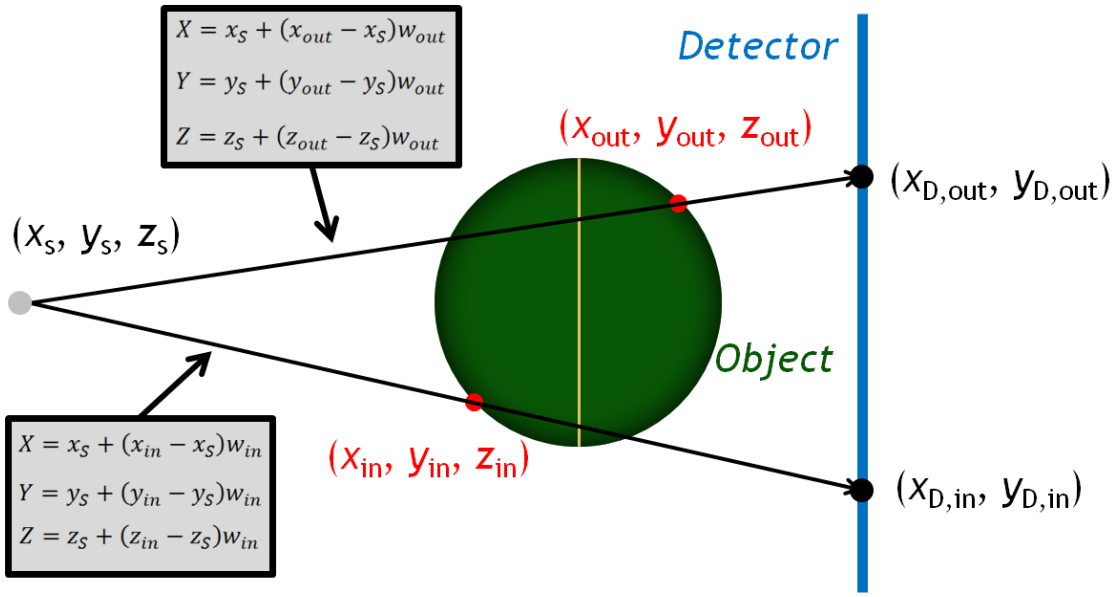

Figure 2.11. The relationship between radiation path lengths and the intersection points of an imaged object. Line equations are made for two groups of points: those closer to the source and those closer to the detector. When lines from both groups map to the same detector pixel ($x_{D,out}$, $y_{D,out}$)= ($x_{D,in}$, $y_{D,in}$) their difference in source to object length corresponds to the path length through the material.

The path length calculation works by dividing the surface points into two groups: points closer to the source (x_{in}, y_{in}, z_{in}) and points closer to the detector (x_{out}, y_{out}, z_{out}). A set of parametric equations (Equations 5, 6, and 7) is used to define the line from the source (x_S, y_S, z_S) to a point in the first group.

$$X = x_S + (x_{in} - x_S)w_{in} \quad (5)$$

$$Y = y_S + (y_{in} - y_S)w_{in} \quad (6)$$

$$Z = z_S + (z_{in} - z_S)w_{in} \quad (7)$$

The points in this group represent photon entry locations into the object. Based on different values of the free parameter, w_{in}, different Cartesian coordinates along the line can be determined. Since the z-coordinate of the detector is known from the imaging setup, w_{in} can be found and be used to determine the x and y-coordinates of the detector along the radiation path. This process is repeated for each pixel in the source side data set. Similarly, the process can be performed for the detector side group of surface points using Equations 8, 9, and 10.

$$X = x_S + (x_{out} - x_S)w_{out} \tag{8}$$

$$Y = y_S + (y_{out} - y_S)w_{out} \tag{9}$$

$$Z = z_S + (z_{out} - z_S)w_{out} \tag{10}$$

As with the first group of surface points, the detector pixel intersecting the line equations of the second group are determined. By combining information from both of these data sets, the entrance and exit point of the incident radiation is known for each detector pixel. Calculating the magnitude of these two vectors and computing the difference gives the path length through the material. Equations 11 and 12 define the magnitude of these line segments.

$$L_{in} = \sqrt{[x_{in} - x_s]^2 + [y_{in} - y_s]^2 + [z_{in} - z_s]^2} \tag{11}$$

$$L_{out} = \sqrt{[x_{out} - x_s]^2 + [y_{out} - y_s]^2 + [z_{out} - z_s]^2} \tag{12}$$

Path lengths are determined for the surface points of each layer. The individual path lengths of the outer layers are determined by subtracting the path lengths of the inner layers. This procedure results in path length maps for each pixel in the image as shown in Figure 2.12.

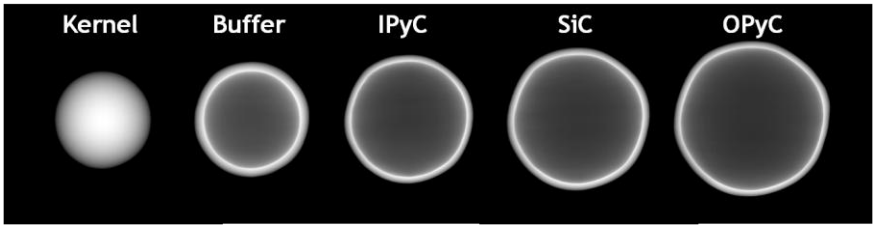

Figure 2.12. Path lengths maps through each individual layer of TRISO fuel. Brighter regions represent a larger path length traversed by the x-rays through the respective layer.

The brighter the pixel in Figure 2.12, the larger the radiation path length was through that material to reach the detector. This data, combined with the energy spectrum data and attenuation coefficient data described in the previous sections fully define the variables required to solve for density.

2.2.4. Density Determination. The information acquired in the previous sections leaves density of the coating layers as the only unknowns in Equation 4. Density is calculated successively through the layers starting with the outermost layer because pixels representing other layers receive photons that have passed through multiple layers and therefore have multiple unknown densities. By finding the density of the OPyC layer, the density of the SiC layer can be determined, and then the IPyC and so forth. The density for the OPyC layer is represented by Equation 13 which is equivalent to Equation 4.

$$I_5 = \sum_{i=1}^{n} I_{0,n} \left(exp \left[- \left(\frac{\mu}{\rho} \right)_{i,5} t_5 \right] \right)^{\rho_5} \tag{13}$$

Density is a constant contained in every term of the summation shown in Equation 13. To determine the left side of the equation, the proportionality of pixel gray value and radiation intensity is utilized, as represented in Equation 14.

$$P_5 = cI_5 \tag{14}$$

Combining these expressions gives the expression in Equation 15.

$$P_5 = c\sum_{i=1}^{n} I_{0,n}\left(exp\left[-\left(\frac{\mu}{\rho}\right)_{i,5} t_5\right]\right)^{\rho_5} \quad (15)$$

To determine the constant of proportionality, *c*, the background of the image is utilized. Since photon attenuation in the background region is negligible, the detector pixels constituting the background of the image receive all of the incident photons. Equation 16 shows how the same constant of proportionality from Equation 15 can be used to equate the background pixel gray level to the radiation intensity.

$$P_{BG} = c\sum_{i=1}^{n} I_{0,n} \quad (16)$$

Dividing Equations 15 and 16 eliminates the constant of proportionality, producing Equation 17.

$$\frac{P_5}{P_{BG}} = \frac{\sum_{i=1}^{n} I_{0,n}\left(exp\left[-\left(\frac{\mu}{\rho}\right)_{i,5} t_5\right]\right)^{\rho_5}}{\sum_{i=1}^{n} I_{0,n}} \quad (17)$$

Since density is embedded in the exponent of each term of the right hand side of the equation, an iterative process is used to determine density. Equation 18 establishes a function *Q* to determine the roots and determine density.

$$\mathrm{Q}(\rho_5) = \frac{\sum_{i=1}^{n} I_{0,n}\left(exp\left[-\left(\frac{\mu}{\rho}\right)_{i,5} t_5\right]\right)^{\rho_5}}{\sum_{i=1}^{n} I_{0,n}} - \frac{P_5}{P_{BG}} = 0 \quad (18)$$

Using the Newton-Raphson method, the density value satisfying the condition *Q=0* is determined. The Newton-Raphson method is illustrated in Equation 19.

$$\rho_{5,m+1} = \rho_{5,m} - \frac{\mathrm{Q}(\rho_5)}{\mathrm{Q}\prime(\rho_5)} \quad (19)$$

The result of this process is a map of density values for each pixel of the outer layer. Depending on the image size, this can correspond to hundreds or thousands of calculated density values. Since the coating layer is assumed to be homogeneous, a representative density value for the entire layer is determined. All radiographs are susceptible to some degree of noise which means no single calculation of density can be determined accurate. Fortunately, the noise in radiographs tends to be low mean, Gaussian noise so the number of outliers is very similar on the bright and dark ends of the spectrum. The set of density calculations is condensed by cropping an equal percentage of outliers off each end and averaging the remaining data points.

Once the density for the OPyC layer is determined, Equation 20 can be used to find the density for the SiC layer.

$$I_{4,5} = \sum_{i=1}^{n} I_{0,n} \left(exp \left[- \left(\frac{\mu}{\rho} \right)_{i,5} t_5 \right] \right)^{\rho_5} \left(exp \left[- \left(\frac{\mu}{\rho} \right)_{i,4} t_4 \right] \right)^{\rho_4} \quad (20)$$

In this manner the density can be determined for every coating layer, simply by adding additional constant terms as the layers are progressed through. The full form of the density algorithm is in Appendix B.

2.3. COMPUTER SIMULATIONS

As part of the validation of the algorithm, simulated images of TRISO fuel were generated. Testing the algorithm with simulated images has several advantages that can't be replicated by experimental images. First and foremost, by virtually creating the object, imaging setup and photon energy spectrum, any sort of image can be produced quickly and easily. Furthermore, the input isn't susceptible to hardware faults. Finally, precision in simulated calculations is absolute, so errors in results cannot be from experimental faults.

The gray levels of the image pixels for the simulated images were formed by analytically solving the Beer-Lambert Law. Attenuation coefficients and x-ray energy spectra were determined from the same sources as described in Section 2.2. To determine

the path lengths in the simulated image, a perfectly spherical geometry was used to represent the TRISO fuel and line segments drawn from the source to detector were used to determine the entrance and exit points of the fuel. By solving for the intersections between a sphere and line segment, a quadratic equation results of which the roots can be determined by Equation 21.

$$L = \frac{-b \pm \sqrt{b^2 - 4ac}}{2a} \tag{21}$$

$$a = (x_D - x_S)^2 + (y_D - y_S)^2 + (z_D - z_S)^2$$

$$b = 2[(x_D - x_S)(x_S - x_O) + (y_D - y_S)(y_S - y_O) + (z_D - z_S)(z_S - z_O)]$$

$$c = x_S^2 + x_O^2 + y_S^2 + y_O^2 + z_S^2 + z_O^2 - 2(x_S x_O + y_S y_O + z_S z_O) - r^2$$

The locations of the source (x_S, y_S, z_S), object (x_O, y_O, z_O), and detector (x_D, y_D, z_D) are all variables in the image generation code which allows for any degree of image magnification and translation to be specified. Additionally, the size of the object can be changed by altering the radius parameter, *r*. To more accurately represent true radiographs, Gaussian noise can also be added to the images. The full algorithm is in Appendix B. Three examples of the same object under different simulated imaging parameters are shown in Figure 2.13.

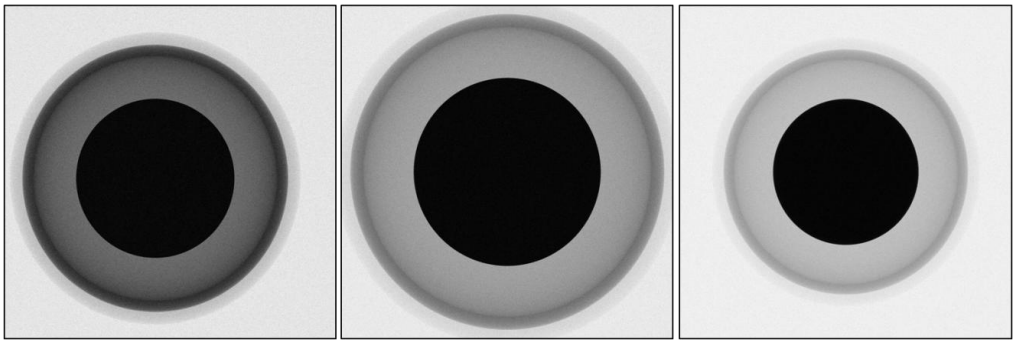

Figure 2.13. Simulated TRISO fuel images. The left image was taken at 20 KVp, 1.1 times magnification, and has 0.0837 mean noise. The center image was taken at 35 KVp, 1.3 times magnification, and has 0.0707 mean noise. The right image was taken at 50 KVp, 1.01 times magnification, and has 0.0548 mean noise. All of the noise values are determined based on image gray levels in the range 0 to 1.

2.4. EXPERIMENTS

To fully validate the algorithm, a radiography experiment was performed. The experiment was performed in the Missouri S&T reactor with the newly established x-ray radiography system. A phantom made of three layered materials was created to test with.

2.4.1. Phantom Design. The design of the phantom needed to be such that density could be determined in a layered object with similar attenuation properties to that of TRISO fuel. The micro-size and involved manufacturing methods of actual fuel proved to be beyond the capacity of this research. To verify the fundamentals of the algorithm, a larger scale, cylindrical phantom was constructed. This proved useful in two ways: the phantom could be constructed using machining tools and it was large enough to work in conjunction with the imaging system at Missouri S&T.

Phantom materials were selected so that the visually obvious differences between TRISO fuel and the phantom had little effect on the density calculation and validation of the algorithm. The phantom, shown in Figure 2.14, is made of three concentric cylinders of zirconium, graphite, and aluminum.

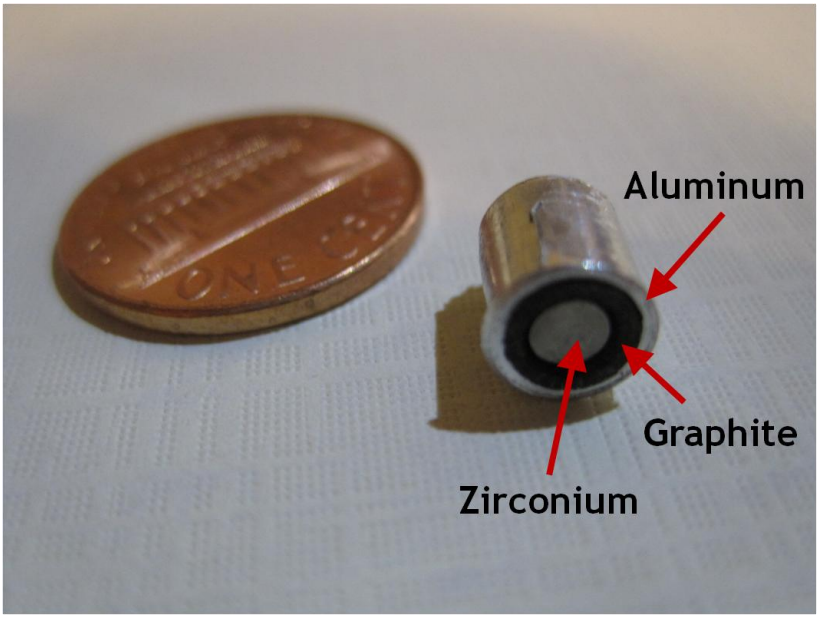

Figure 2.14. The cylindrical fuel phantom made of zirconium, graphite, and aluminum.

The outer diameter of the fuel phantom is 0.61 cm, roughly 6 times larger than most TRISO fuel particles. Zirconium is used because of its density; like uranium oxides and carbides, zirconium is highly attenuating. Graphite and aluminum were selected as pseudo materials for pyrocarbon and silicon carbide, respectively, because of the closeness in their attenuation coefficients.

2.4.2. Experimental Setup. The x-ray radiography experiment was performed using the newly created system in the Missouri S&T Reactor. Figure 2.15 highlights the x-ray components of the system.

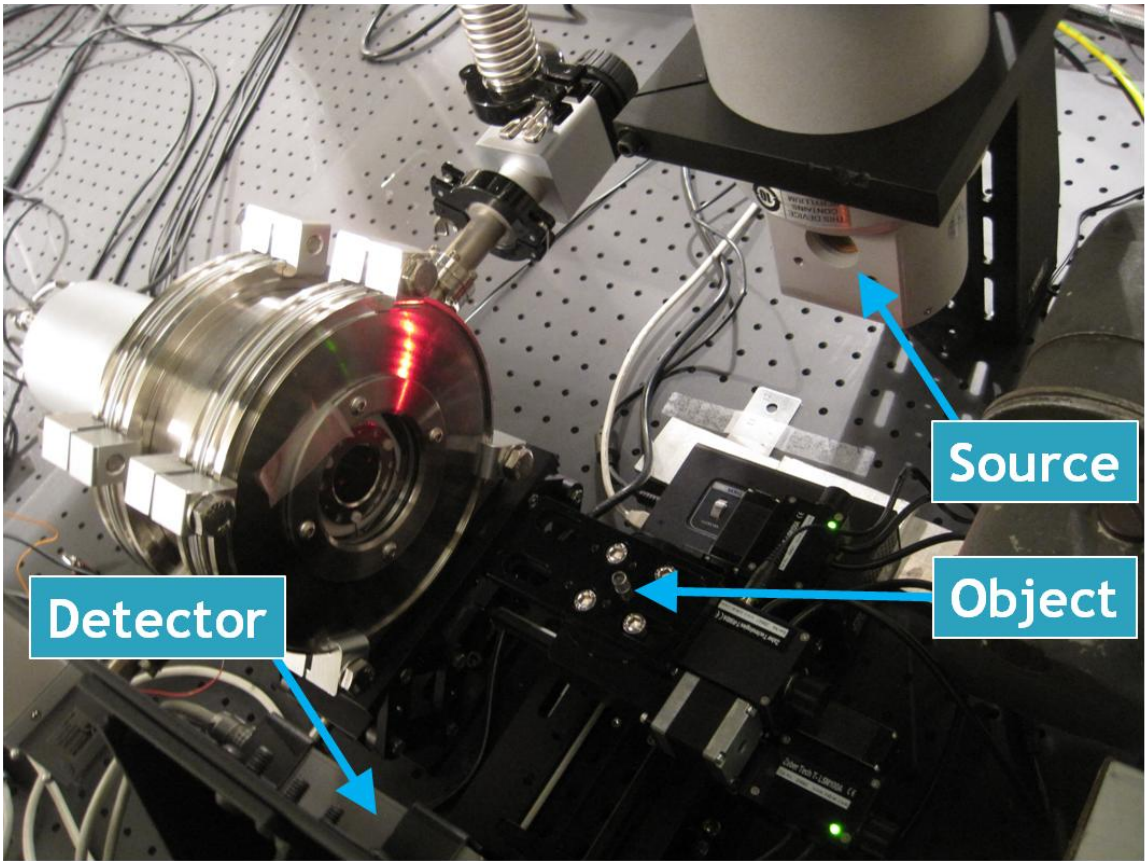

Figure 2.15. The experimental setup used.

The object is positioned on motorized stages which allow rotation and translation of the object. The parameters in Table 2.2 were used for the experiment.

Table 2.2. Experimental setup and acquisition parameters.

Magnification	2
Source to detector distance	44 cm
Object to detector distance	22 cm
KVp	50
Focal Spot	0.4 mm
X-ray tube current	0.7 mA
Exposure time	1200 ms

Specifications of the x-ray sensor and x-ray generator are in Appendix C.

2.4.3. Image Processing. The radiograph set that was taken consisted of eight pairs of radiographs taken at equal azimuth angle increments from 0° to 180°, eight bright images, and a dark image. After taking the images, they needed to be corrected to account for dead pixels and background effects. To correct the dead pixels, they were first located by thresholding a background image and then reassigned values by interpolating pixels in their neighborhood.

Even in a blank radiograph without an object, differing response of photodiodes, electrical disturbance, and uneven illumination of detector pixels produces a non-uniform image. Flat-field correction corrects this problem by utilizing bright and dark images. For this experiment, bright images (B) were taken with the same conditions listed in Table 2.2 without the object present and a dark image (D) was taken while the x-ray generator was off. Utilizing Equation 22, flat-field correction was applied to improve the raw radiograph (R).

$$F = \frac{R-D}{B-D} \tag{22}$$

Flat-field correction performs a vital function by artificially equalizing the number of photons incident upon each pixel. This result makes the initial photon intensity a constant for every pixel calculation in Section 2.2.4. Figure 2.16 shows the improvement made by applying flat-field correction.

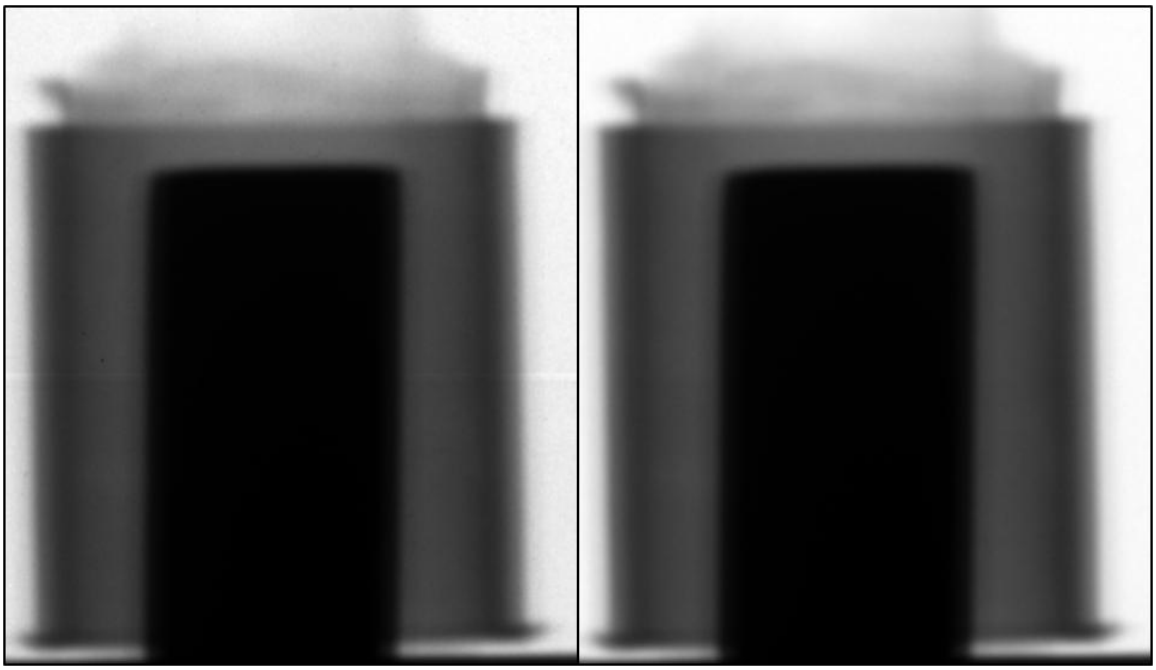

Figure 2.16. Radiograph region of interest before (left) and after (right) processing.

To display the image imperfections that are only a few pixels in size, a small region of the image is shown in Figure 2.16. The most noticeable effect in the region of interest shown is the bright horizontal line artifact running through the center of the phantom. The uniformity of the background is also improved. On the portion of the background not shown in Figure 2.16, similar line artifacts as well as blotches were corrected.

3. RESULTS AND ANALYSIS

Results obtained from both simulated and experimental methods are presented in this section. All of the results were derived from the algorithm presented in Section 2.2. The simulated results include density calculations with ideal and non-ideal inputs. Sensitivity studies were performed with respect to image noise, x-ray generator voltage fluctuations, and statistical processing of the data for several x-ray generator voltage settings. The results from the experiment are shown and sources of error, such as radii measurement perturbations and x-ray generator photon energy distribution fluctuations are analyzed.

3.1. SIMULATED RESULTS AND ANALYSIS

The simulated images that were generated without noise represent an ideal radiograph in which the imaging parameters are known with certainty. From these radiographs, density was determined with almost no error. Table 3.1 shows the density calculation results for a simulated image generated with 30 KVp.

Table 3.1. Density calculation and error for a simulated image generated with 30 KVp.

Layer	Actual Density	Calculated Density	Error (%)
Buffer	1.100	1.099	0.0675
IPyC	1.900	1.902	0.0914
SiC	3.180	3.180	0.0017
OPyC	1.900	1.899	0.0512

The results show that in the idealized case, the utilized method can precisely determine density of all the coating layers. The slight amount of error is due to the finite size of the image pixels and finite number of gray levels a pixel can have.

Several sensitivity studies were performed to evaluate how the algorithm handles uncertainty and imprecision. First, the effect of noise on the density calculation was evaluated. This was done by generating a set of simulated images in which all the parameters except for the magnitude of noise remained constant. The density calculations and comparisons for these noisy images are outlined in Table 3.2. The images used were generated at 20 KVp with a 0.8 cm thick beryllium filter and 11 degree tungsten anode target angle.

Table 3.2. Noise effects on the density calculation when 25% of the data is cropped from each end. The variance of noise is determined based on gray values in the range 0 to 1.

Layer	**Actual Density (g/cm^3)**	**Calculated Density (g/cm^3)**							
		Variance of Noise							
		0.001	**0.003**	**0.005**	**0.007**	**0.009**	**0.011**	**0.020**	**0.030**
Buffer	1.1	1.096	1.100	1.114	1.080	1.076	1.095	1.089	1.032
IPyC	1.9	1.913	1.885	1.903	1.853	1.896	1.835	1.834	1.856
SiC	3.18	3.183	3.195	3.201	3.219	3.225	3.238	3.277	3.332
OPyC	1.9	1.903	1.915	1.916	1.916	1.932	1.940	1.970	2.008
		Error (%)							
Buffer		0.383	0.017	1.232	1.849	2.214	0.471	0.959	6.180
IPyC		0.678	0.807	0.181	2.465	0.231	3.406	3.452	2.322
SiC		0.107	0.465	0.669	1.236	1.416	1.820	3.045	4.770
OPyC		0.164	0.772	0.822	0.865	1.690	2.141	3.664	5.698

The variance values in Table 3.2 are specified for an image with gray values between 0 and 1. Noise variance for images used in this paper are less than 10^{-6} The statistical approach of the algorithm was anticipated to be particularly well suited to handle the low-mean Gaussian noise which commonly accompanies x-ray radiographs because the statistical nature of noise all but assures that for every pixel that has an intensity below the mean, a sister pixel with an intensity above the mean exists. Interestingly, Table 3.2 shows a strictly increasing value for the density of the OPyC and

SiC layers despite the statistical nature of the noise. This can be explained by the nature of the complete set of density calculations. If you were to order the calculated values of density for every pixel in ascending order, the plot would follow a cubic curve; there are outliers that cause large slopes on the edges as well as data points clustered toward the true value. Figure 3.1 illustrates this point graphically. The slope of the graph increases with the magnitude of noise.

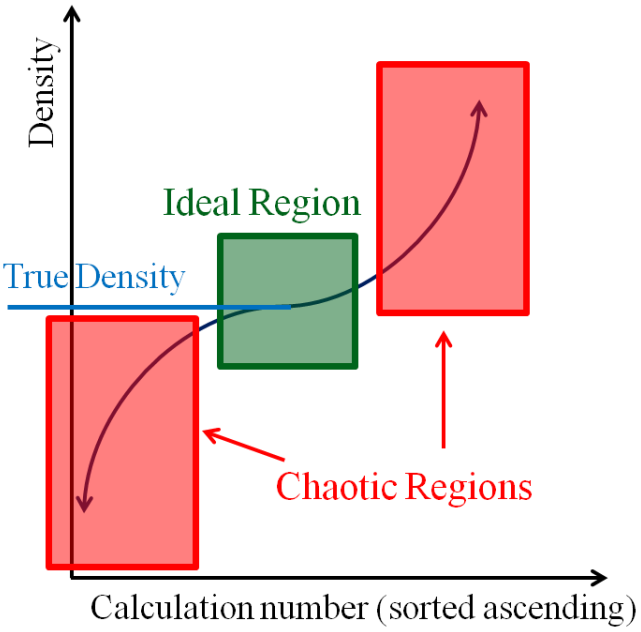

Figure 3.1. Sorted plot of density values affected by Gaussian noise. This curve represents the distribution of density values resulting from noise overestimating and underestimating some values, creating the chaotic regions. Each data point on the x-axis corresponds to a calculation performed at a pixel in the image.

In the case of pure symmetry, it would be acceptable to include data from the chaotic regions. However, a slight deviation from symmetry would introduce outliers that are far from the median. This explains the increasing trend in the densities shown in Table 3.2.

The data in Table 3.2 corresponds to 25% of the total pixel measurements for each coating layer being excluded in from the mean. By cropping data, the pixel values that are most radically affected by noise are excluded. Table 3.3 displays results with 45% of the data cropped from each end.

Table 3.3. Noise effects on the density calculation when 45% of the data is cropped from each end. The variance of noise is determined based on gray values in the range 0 to 1.

Layer	**Actual Density (g/cm^3)**	**Calculated Density (g/cm^3)**							
		Variance of Noise							
		0.001	**0.003**	**0.005**	**0.007**	**0.009**	**0.011**	**0.020**	**0.030**
Buffer	1.1	1.095	1.107	1.135	1.093	1.102	1.115	1.133	1.092
IPyC	1.9	1.917	1.884	1.895	1.845	1.884	1.859	1.857	1.917
SiC	3.18	3.179	3.182	3.177	3.188	3.186	3.183	3.182	3.187
OPyC	1.9	1.900	1.905	1.901	1.890	1.898	1.904	1.900	1.898
		Error (%)							
Buffer		0.424	0.650	3.181	0.667	0.150	1.365	3.025	0.744
IPyC		0.898	0.857	0.283	2.913	0.824	2.149	2.287	0.911
SiC		0.043	0.055	0.093	0.261	0.200	0.082	0.069	0.205
OPyC		0.016	0.242	0.065	0.551	0.084	0.200	0.007	0.095

With a larger number of values discarded as outliers, the measurement error decreases. Furthermore, a clear relationship between noise variance and density ceases to exist. This indicates that all of the data from the chaotic region in Figure 3.1 has been excluded and the slight asymmetry of the curve no longer skews the results. Furthermore, the relationship between noise variance and error has been eliminated. This means that even with extreme levels of low-mean noise, the algorithm can accurately extract density.

For all values of variance in Tables 3.2 and 3.3 the error was less when 45% of data was cropped than 25%. To characterize this effect more thoroughly, the effect of changing the magnitude of cropped data for a fixed noise variance was analyzed, the

result of which is shown in Figure 3.2. The variance for each case was kept at 0.007 which is measured for gray levels in the intensity range from 0 to 1.

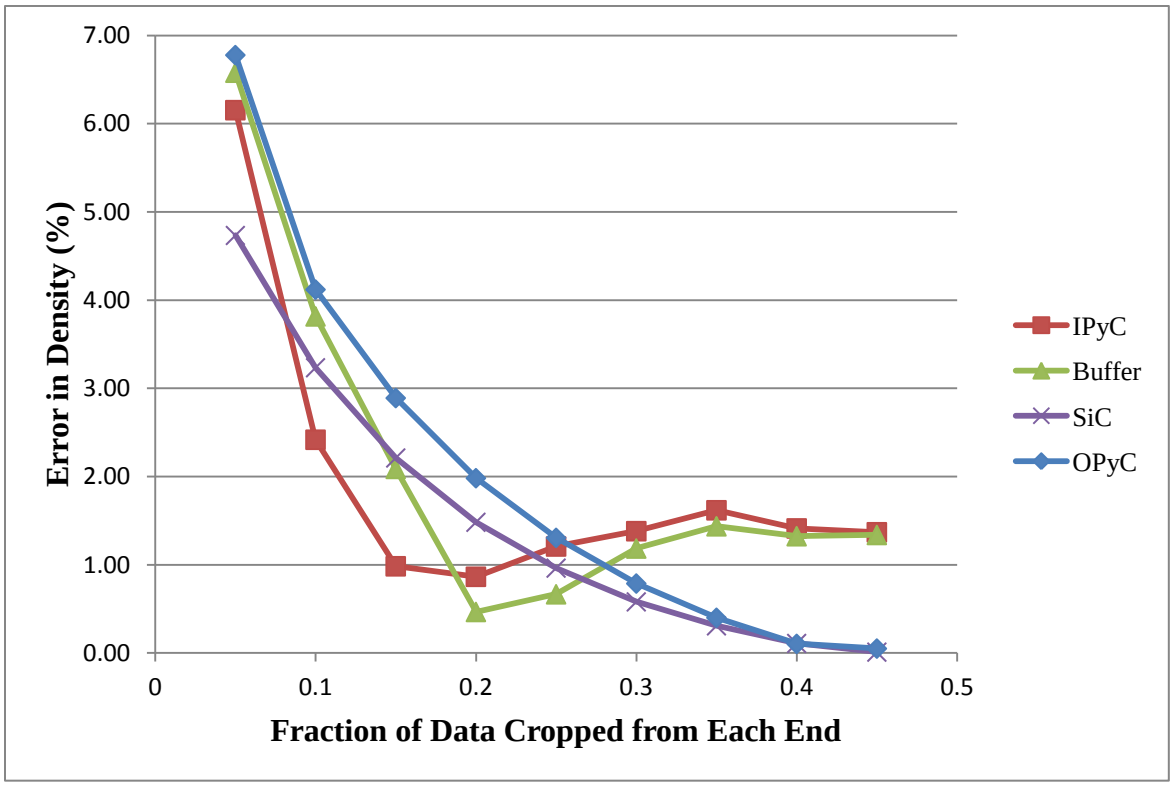

Figure 3.2. Effect of the crop limit on density error.

The curves for the outer two coating layers illustrate that as more of the unstable, noisy data points are excluded from the calculation, the error reduces. This effect is asymptotic and has diminishing returns as more data is removed. The curves for the IPyC and buffer layers have local minima at 20% caused by the interdependence of the coating layer densities; the error in the OPyC and SiC density measurements caused by noise counteracts the noise incurred in the IPyC and Buffer layers. Likewise, the local maxima of the IPyC and buffer layers when 35% of the data is cropped are caused by constructive interference between the error in the outer layers and noise.

In an effort to reduce noise, large fractions of data should be cropped from the data set so the data more closely represents a median rather than a mean. Based on Figure 3.2, the cumulative error for all of the coating layers is nearly as low when 28% of the data is cropped then when 45% is cropped but this result is exclusive to the parameters used for this data set. To ensure consistency over a variety of imaging conditions, cropping larger fractions of data is a better method.

X-ray generators rely on precise voltage levels to produce a consistent photon source. Although voltage is typically well controlled, slight deviations are possible. To analyze this effect, x-ray spectra for different voltage settings were generated using SpekCalc and utilized in the algorithm with an image generated at a single voltage setting. For the case of an image generated with 20 KVp, the results are shown in Figure 3.3.

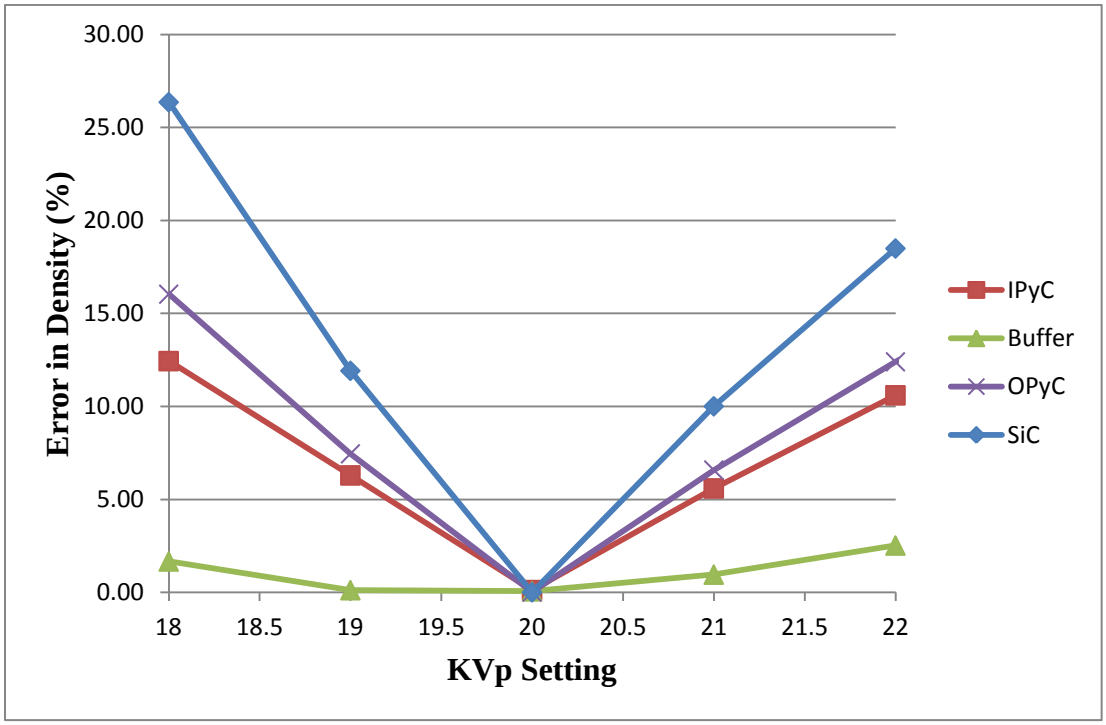

Figure 3.3. The effect of voltage imperfections on density error for the 20 KVp case. The results were obtained by generating an image with 20 KVp and performing the calculation as if the KVp was the value on the x-axis.

What Figure 3.3 shows is if an x-ray system is specified to run at one of the KVp settings on the x-axis but in reality produces a 20 KVp spectrum, what the resulting error will be. At the voltage ranges used in this paper, a 0.5 KVp error would be rather egregious. In reality, the spectrum is more likely to vary up to 0.1% of the KVp setting.

As expected, the more the spectrum deviates from the true value, the higher the resulting error in density. Similar to the analysis of the crop limit, the propagation of error through the layers can act constructively or destructively with the error incurred from voltage inaccuracy. For this case, the error in the buffer layer is destructively reduced by error propagation whereas SiC suffers from constructive error interference.

For a realistic offset of voltage in the 20 KVp case, an error of less than 0.5% can be expected to be introduced into the density calculation. This study was repeated with higher KVp cases; the results for 40 KVp are shown in Figure 3.4. The higher KVp case has a lower overall magnitude of error caused by the same voltage displacement.

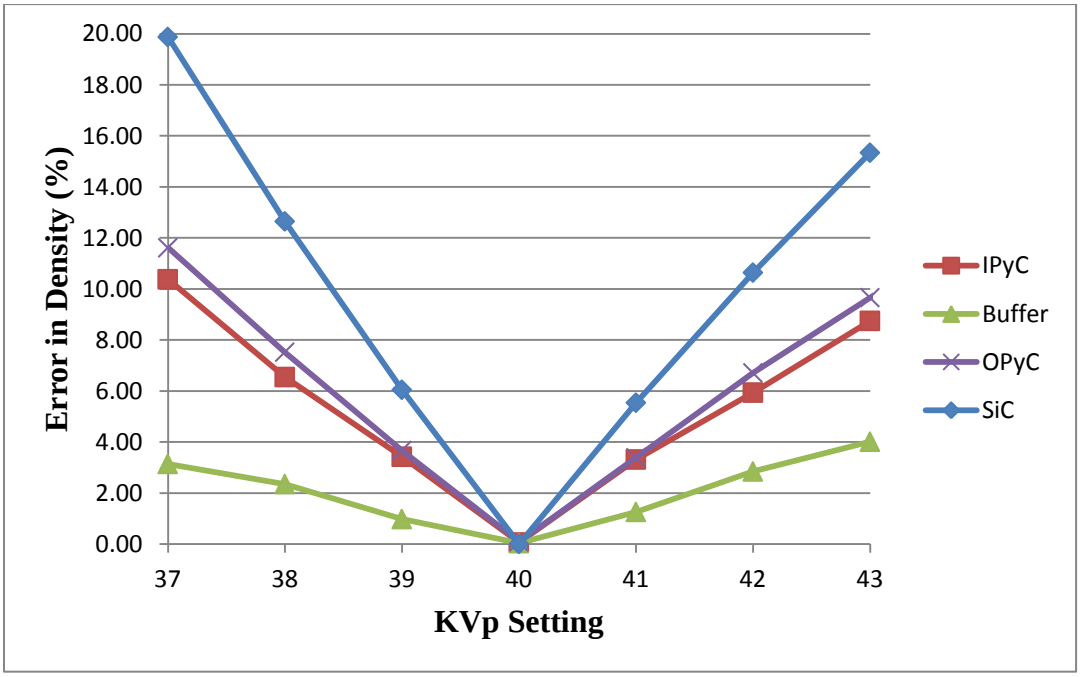

Figure 3.4. The effect of voltage imperfections on density error for the 40 KVp case.

3.2. EXPERIMENTAL RESULTS AND ANALYSIS

As a point of comparison, density was determined for simulated images that were generated with the same parameters as the experiment. Both image types are shown in Figure 3.5.

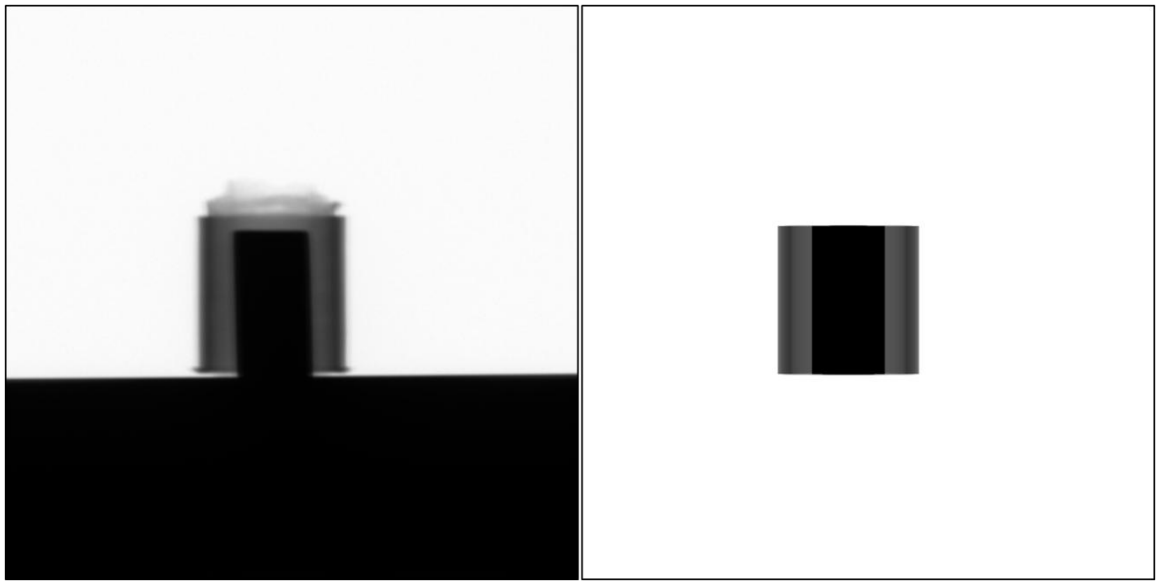

Figure 3.5. A comparison of an actual radiograph (left) and a simulated image (right) that were acquired using identical parameters.

The black on the bottom portion of the actual radiograph is the stage the phantom is sitting on. It is clear from the figure that the simulated and actual images are similar although the actual image has some imperfections. Three factors competed to mitigate these factors in the design of the experimental setup:

- the object size needed to be sufficiently small to reduce the ratio of scattering interactions to absorption interactions,
- the magnification needed to be chosen to maximize the effective pixel size without causing too much blurring in the image,

- and the source to detector distance needed to be sufficiently large compared to the focal spot size to maximize the discernable size of image features.

Taking into account these three factors, the parameters in Table 2.2 were defined. Unfortunately, limitations of the system necessitated compromise to generate a meaningful image. If the image was magnified further, the blurring would be amplified and make the layer boundaries more difficult to discern.

The small size of the image on the detector leads to problems with measuring coating layer thicknesses. Radii measurements are limited by the size of the detector pixel and geometric magnification. Since the pixel size for the detector used in this experiment is 48 microns and the magnification is 2, radii measurements are limited to increments of 24 microns. This relatively large detector pixel size for the size of the object leads to imperfections even with the smallest of measurement errors. Table 3.4 shows the effect slight errors in radii measurements have on calculated density values for simulated images generated under the same conditions as the experiment.

Table 3.4. The effect of boundary layer offset on density error. The offset is defined as the number of pixels away from the true value where negative represents an offset toward the center of the object and positive is away from the center of the object.

Layer	**Actual Density (g/cm^3)**	**Calculated Density (g/cm^3)**						
		Aluminum Layer Pixel Offset						
		-3	**-2**	**-1**	**0**	**1**	**2**	**3**
Kernel	6.506	6.563	6.563	6.563	6.563	6.563	6.563	6.563
Carbon	1.74	1.627	1.686	1.807	1.751	1.698	1.857	1.966
Alum.	2.7	3.092	2.943	2.774	2.691	2.613	2.459	2.347
		Error (%)						
Kernel		0.876	0.876	0.875	0.876	0.879	0.876	0.876
Carbon		6.471	3.115	3.833	0.632	2.437	6.730	12.966
Alum.		14.504	9.011	2.756	0.333	3.237	8.911	13.067

In the analysis, the boundaries marking the outside of the kernel and carbon layers were fixed and the outside diameter of the aluminum layer was adjusted in increments of one pixel. The negative offsets in Table 3.4 correspond to a decrease in diameter and the positive offsets correspond to an increase in diameter. The data shows that even small perturbations in the measurement of the coating layers have a rather severe impact on calculated density values. Compared to the errors introduced due to image noise, x-ray generator voltage fluctuations, and statistical processing, the error caused by coating layer measurement fluctuations can have a profound effect. To get a realistic idea of what the offset will be for an image, several factors must be considered.

The boundaries between layers in an image are defined by steep gray level transitions. Larger focal spot sizes, higher levels of image magnification, and larger pixel sizes tend to obscure these transitions, making the boundary a smooth transition rather than a sharp one. Several things can be done to remedy this effect, such as decreasing the focal spot size, decreasing the detector pixel size, and reducing the level of magnification. It is apparent that this effect is dependent on the imaging system used and this error can be mitigated by improving the system.

In addition to error caused by offset radii measurements, the error due to photon energy distribution fluctuations was investigated. Section 3.1 discussed the error to the spectrum related to voltage fluctuations whereas this study is focused on fluctuations of the spectrum when voltage remains constant. As such, this study is a measure of discrepancies between the spectrum generated by the x-ray tube and the spectrum generated by the SpekCalc program. It is impossible to characterize all of the possible fluctuations to the energy spectrum; for this study, alterations to the energy distribution were made by filtering the beam with aluminum filters of varying thicknesses. The impact these spectra variations had on density is shown in Table 3.5.

Table 3.5. The effect altering the photon energy distribution has on calculated density values. Alterations to the spectrum were made by inserting aluminum filters of varying thickness.

Layer	Actual Density (g/cm^3)	Calculated Density (g/cm^3)							
		Aluminum Filter Thickness (mm)							
		0.00	**0.01**	**0.03**	**0.05**	**0.10**	**0.15**	**0.20**	**0.30**
Kernel	6.506	6.563	6.564	6.565	6.566	6.568	6.570	6.571	6.574
Carbon	1.74	1.751	1.849	2.011	2.138	2.361	2.507	2.622	2.760
Alum.	2.7	2.691	2.770	2.901	3.008	3.224	3.396	3.536	3.780
		Error (%)							
Kernel		0.88	0.89	0.91	0.92	0.95	0.98	1.00	1.04
Carbon		0.63	6.26	15.55	22.90	35.67	44.09	50.70	58.63
Alum.		0.32	2.58	7.44	11.42	19.42	25.76	30.95	40.00

The results in Table 3.5 mean little without understanding how the spectrum changes based on different filter thicknesses. To better quantify the results, Figure 3.6 shows a comparison between some of the tested spectra and Table 3.6 shows a comparison of the average photon energies of each spectum.

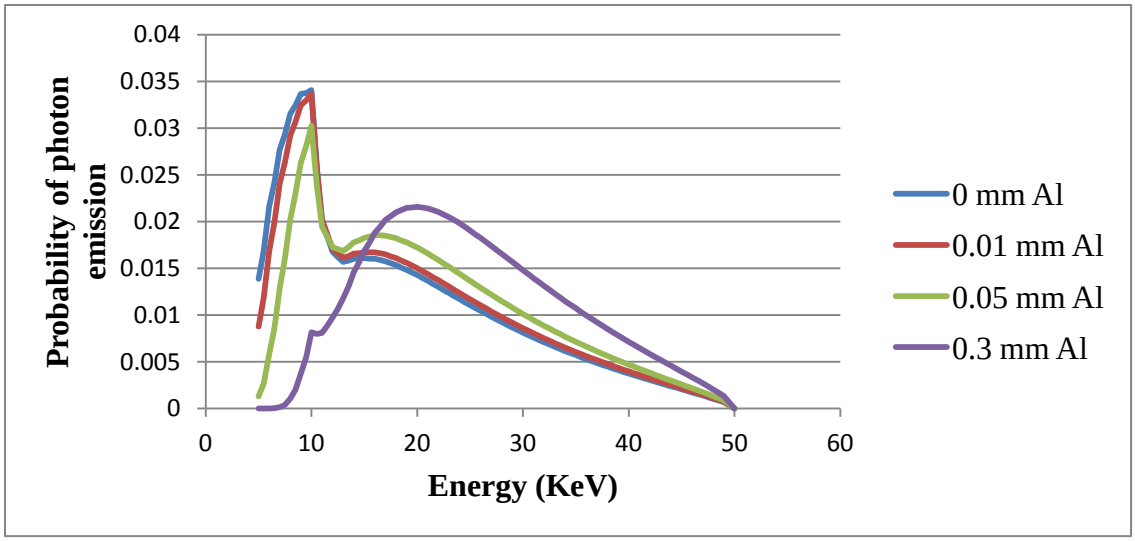

Figure 3.6. Normalized energy spectra generated with varying levels of aluminum filtration.

Table 3.6. Comparison of the average energies of the spectra in Figure 3.6.

Al Filter Thickness (mm)	Average Spectrum Energy (KeV)	Percent Difference from Unfiltered Case
0.00	20.14	0.00
0.01	20.81	3.31
0.05	22.79	13.16
0.30	27.73	37.65

The curves in Figure 3.6 are normalized by the total number of emitted photons; in reality, fewer photons would be emitted in the higher filter cases. For higher filter thicknesses, beam hardening becomes more significant and the average photon energy increases, seen in Table 3.6.

The data shows that the filter thicknesses used in the analysis cover a large range of photon energy distributions. As such, the large errors reported in Table 3.5 for larger filter thicknesses are understandable. Comparing Table 3.5 and Table 3.6, it can be seen that the percent difference in energy between the original spectrum and altered spectrum is closely related to the error in the outer coating layer density calculation. The spectra generated by SpekCalc were compared to an alternate spectrum calculation program (IPEM78) and a Monte-Carlo code (BEAMnrc) using several standards, including the average energy [24]. In both of these comparisons for a 50 KVp test case, the discrepancy was 0.31%. These results were obtained from tests which were performed with a 2.5 mm aluminum filter and a 10 degree target angle. The tube used in this experiment has a 0.8 mm beryllium filter and has an 11 degree target angle. The minor discrepancy in average energy in these tests is anticipated to apply to the x-ray generator at Missouri S&T.

Among the sources of error discussed, the coating layer radii measurement is dominant. As such, the results of the density calculation are presented along with density measurements at offset values. Table 3.7 shows the results obtained from the experiment images.

Table 3.7. Experimentally calculated coating layer density at the predicted boundary location and offset locations.

Layer	Actual Density (g/cm^3)	Calculated Density (g/cm^3)						
		Aluminum Layer Pixel Offset						
		-3	-2	-1	0	1	2	3
Carbon	1.74	0.800	1.112	1.388	1.588	1.772	1.950	2.141
Alum.	2.7	3.260	3.065	2.897	2.762	2.642	2.533	2.429
		Error (%)						
Carbon		54.046	36.069	20.224	8.713	1.822	12.040	23.046
Alum.		20.722	13.515	7.304	2.296	2.144	6.189	10.026

Density could not be determined for the zirconium core because at 50 KVp, not enough photons could penetrate the layer for the detector to measure the intensity. To determine the density of this layer, the voltage setting of the x-ray generator would need to be increased beyond the optimal operating range for the detector that was used.

For the true boundary layer locations, the aluminum and carbon layer densities were determined to be 1.588 g/cm^3 and 2.762 g/cm^3, respectively. By examining the results obtained at pixel offsets, the strong dependence of the density calculation on coating layer thickness seen from the simulated images is reiterated.

Interestingly, when the boundary for the aluminum layer is increased by one pixel, the density calculation gets closer to the actual value and the errors are only around 2%. However, the uncertainty of this calculation is relatively high.

Inaccuracies in the density calculation result from propagation of a multitude of errors; they are:

- focal spot size,
- detector pixel size,
- imperfect boundary demarcation,
- propagation of error through coating layers,
- error in material density,
- imaging setup geometry errors,
- image noise,

- photon attenuation by air,
- x-ray spectrum imperfections and fluctuations,
- x-ray spectrum energy bin size,
- scattering contribution to the image,
- detector energy response function,
- attenuation coefficient error,
- and pixel dynamic range.

For this experiment, most of these error sources had little to no contribution. The error sources that most drastically affected the experimental results, such as the focal spot size and detector pixel size, were limitations of the imaging system used.

To continue this work, an imaging system which has much smaller effective pixel size than the object size as well as smaller focal spot should be utilized. These changes would reduce the uncertainty in the radii measurements drastically. For inspection of actual TRISO particles, this is highly important because of their small size. Additionally, experiments could be performed with filtered photon energy spectra. This would reduce the low energy photon contribution and reduce some potential sources of error such as x-ray spectrum imperfections and photon attenuation by air.

Simulation work could be continued by adding features to the image generating algorithm. Modifications to the algorithm could be made to account for the finite focal spot size which would allow the degree of blurring to an image to be diagnosed beforehand. Also, additions could be made to incorporate more sample geometries. This would extend the applicability of the algorithm beyond that of TRISO fuel.

4. DISCUSSION

Two main developments have come from this paper:

1. an algorithm that simulates radiographs of spherical and cylindrical objects for any imaging setup,
2. and an algorithm that determines the density of TRISO fuel coating layers.

The use of these developments and their potential applications are discussed in this section and comparisons to other methods are made.

The image generating algorithm can be used to generate simulated images for any projection based imaging system. The algorithm is versatile, allowing the user to specify:

- the x-ray energy spectrum parameters such as KVp and filter materials,
- the number of detector pixels and the detector pixel size,
- imaging geometry dimensions such as source-to-object distance, object-to-detector distance, and source and object offsets from the detector centerline,
- object properties including materials, dimensions and densities,
- and image noise.

As such, the algorithm proved useful for analyzing the density algorithm but also has potential use as a diagnostic tool for radiography experiments. Since the properties of a radiograph are dependent on the interplay of all the parameters listed above, as well as exposure time and x-ray tube current, calculations or experiments are necessary to foresee what the radiograph will look like. The image generating algorithm that was developed consolidates all the necessary calculations and outputs an easy to understand, visual result. As such, imaging parameters can be defined easily before starting experiments without the need to use an actual imaging system. This both saves time and prevents dose.

The method used in the density calculating algorithm is a novel approach. It is an analytical method that stems from simple attenuation properties. Using simulated images, the efficacy of the algorithm was established. Even noisy images and imperfect imaging conditions can be handled with little error. The most critical consideration when using the algorithm is the ability to discern coating layer thicknesses which depends on the relative sizes of the object, focal spot size, and detector pixels. Because these parameters were not

ideal for the imaging system at Missouri S&T, the uncertainty of the density calculations are relatively high. The calculated values were, however, close to the actual values.

The developed method has several advantages over commonly utilized methods such as the sink-float method, computed tomography, and ceramography. All of the mentioned methods are time consuming and the sink-float and ceramography methods are destructive. Using a limited number of radiographs as the proposed algorithm does reduces the time required for analysis significantly. If multiple imaging systems are used simultaneously and the algorithm is expanded to calculate the density of multiple TRISO particles in a single image, throughput of imaged particles could approach the rate necessary for commercial production.

5. CONCLUSIONS

An algorithm capable of determining the density of HTGR fuel pellets has been developed. The density information provided by such means can be utilized as a quality control method. Compared to commonly used quality control methods, this method utilizing radiography can be performed nondestructively and quickly which is a step toward efficacy of quality control for production on a commercial scale.

Testing of the proposed method began with generation of simulated images of spherical coated fuel particles. Testing the algorithm with simulated images showed that under idealized conditions, density can be effectively determined for all of the coating layers using the proposed algorithm. Furthermore, image noise and moderate perturbations of the photon energy spectrum have little effect on the accuracy of calculated density values.

Testing continued on a cylindrical phantom object made of zirconium, carbon, and aluminum. Cylindrical simulated images were generated and the effects of radii measurement perturbations and x-ray generator photon energy distribution fluctuations were characterized. Actual radiographs were generated using the imaging system at Missouri S&T and the resulting density calculations were in agreement with the actual values although the uncertainty of the density is relatively high because of the large size of the x-ray tube focal spot and detector pixels compared to the phantom that was used. Utilizing new hardware, this uncertainty could be drastically reduced.

The simulated image generator allows the user to choose any energy spectrum, detector size, imaging geometry dimensions, object dimensions, and object materials to form a simulated radiograph. As such, it can be used as a tool to establish experimental imaging parameters without using an actual imaging system, both saving time and preventing unnecessary dose.

For this algorithm to be successful with objects less than one millimeter in diameter, an imaging system with a detector which has correspondingly small pixels must be utilized. Accuracy of the density calculation relies on accurate characterizing of the energy spectrum, material attenuation coefficients, and imaging geometry, all of which can be controlled when manufacturing a system for commercial applications.

APPENDIX A.
MATERIAL MASS ATTENUATION COEFFICIENTS

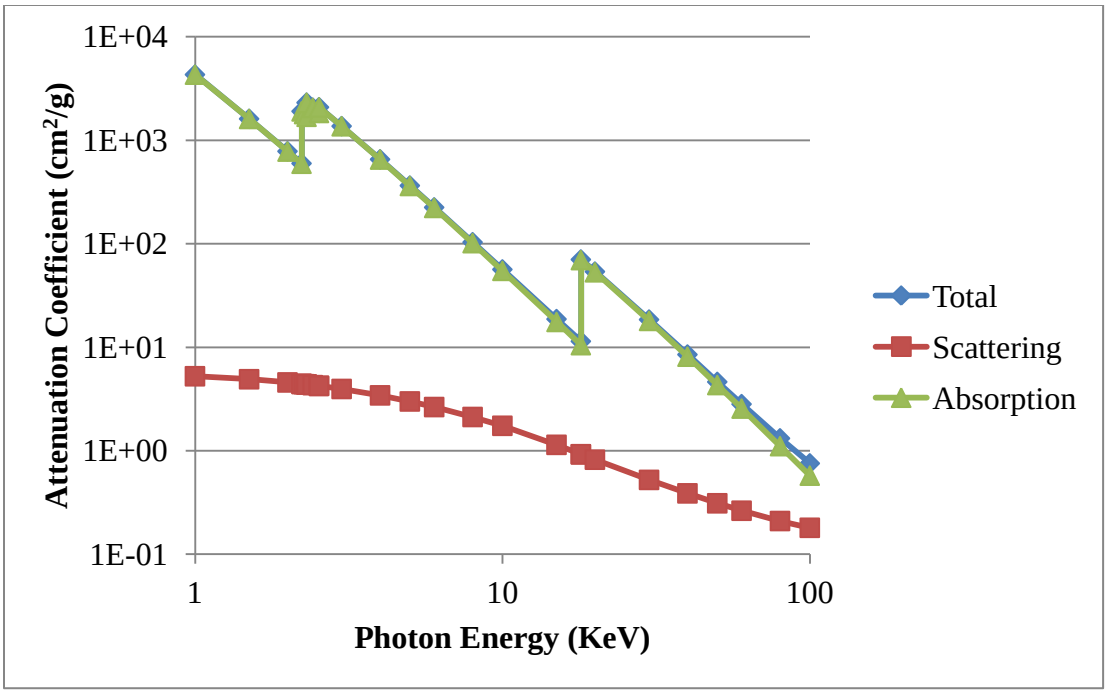

Figure A.1. Mass attenuation coefficient of ZrO_2 for 1 to 100 KeV photons.

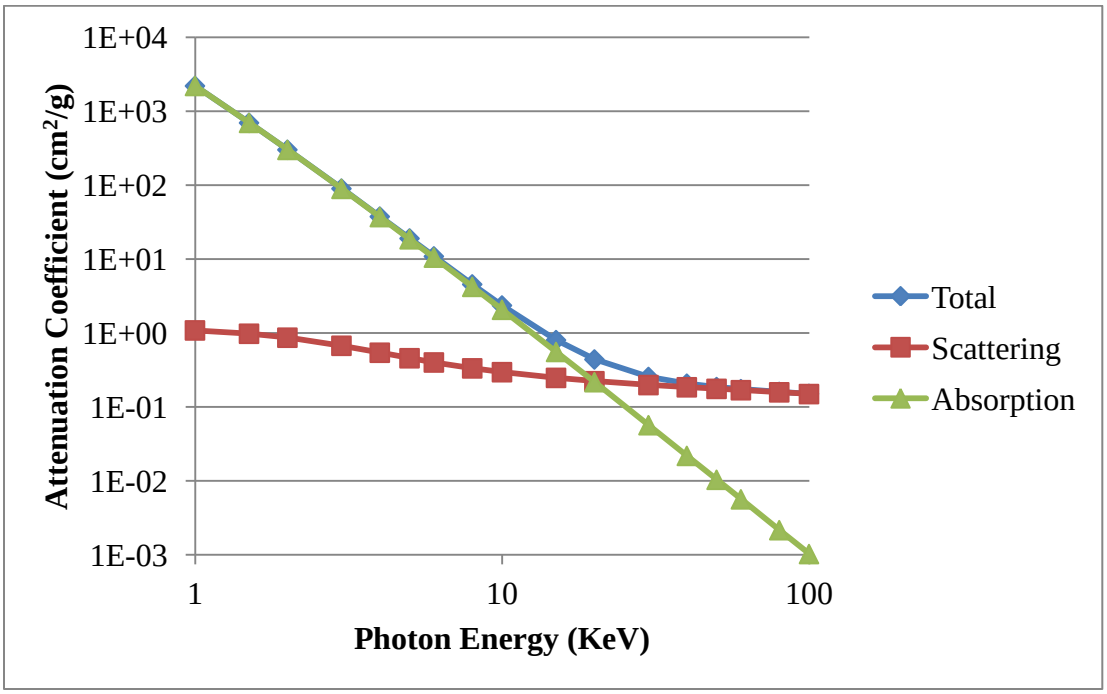

Figure A.2. Mass attenuation coefficient of carbon for 1 to 100 KeV photons.

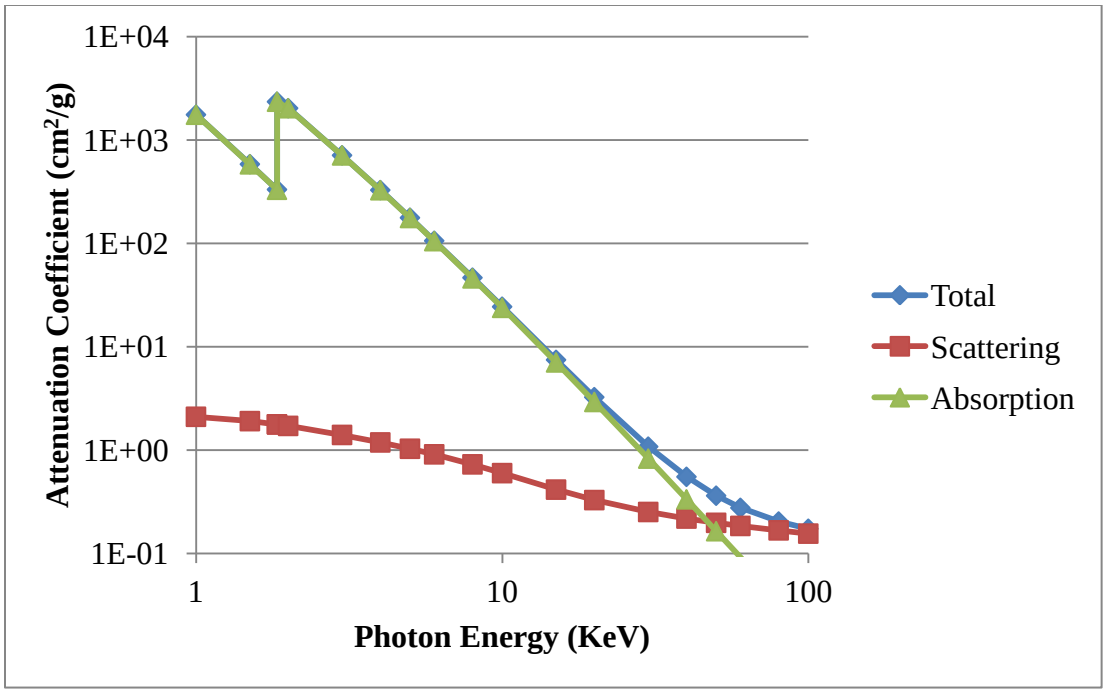

Figure A.3. Mass attenuation coefficient of SiC for 1 to 100 KeV photons.

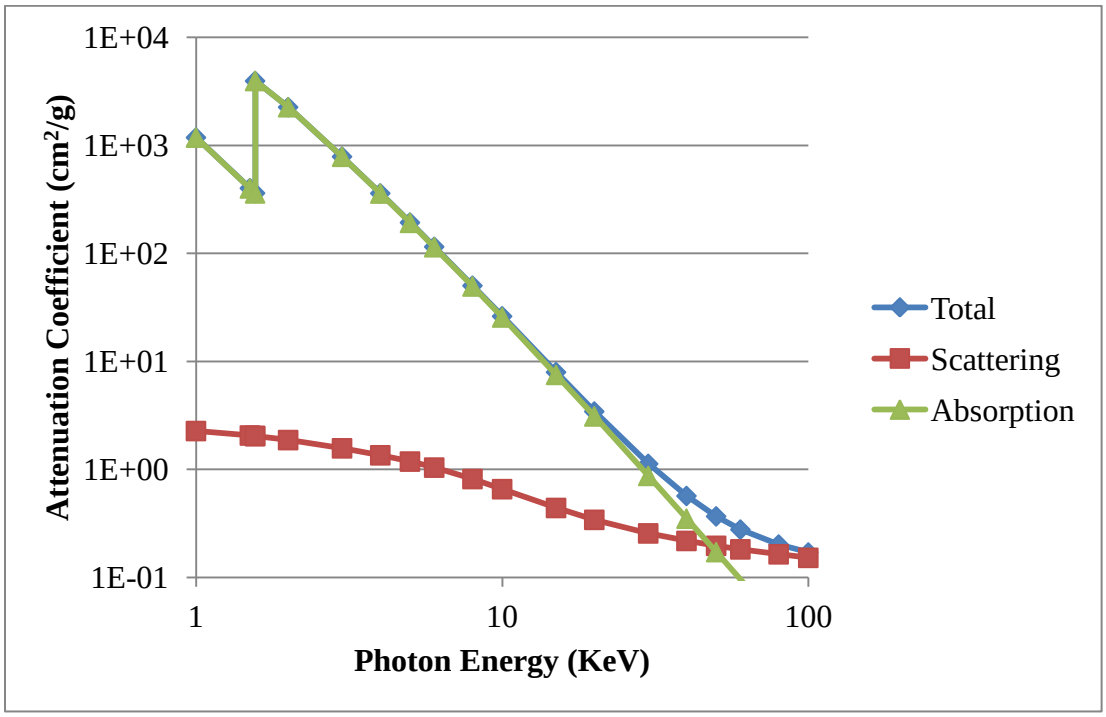

Figure A.4. Mass attenuation coefficient of aluminum for 1 to 100 KeV photons.

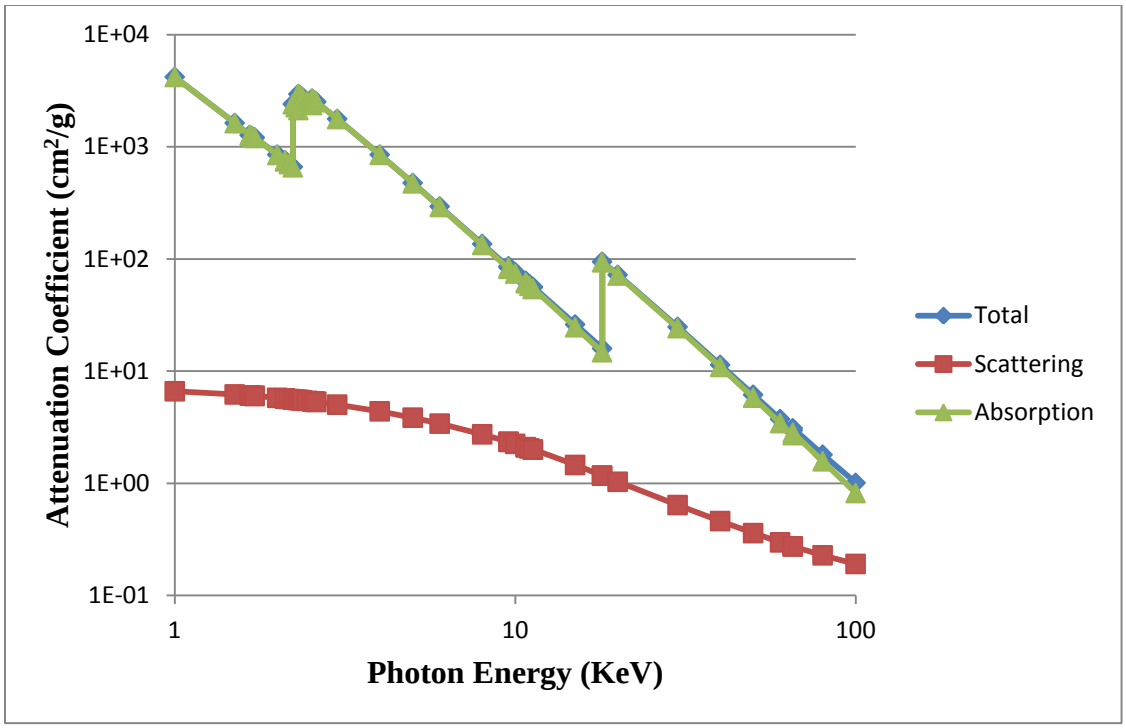

Figure A.5. Mass attenuation coefficient of zirconium with 1.4 atom percent Hafnium for 1 to 100 KeV photons.

APPENDIX B.
MATLAB COMPUTER CODES

```
%% INPUT PARAMETERS %%
close all;clear all;clc;tic
%
Ni=8;       %Total number of radiographs in sample set
N=4;        %Number of radiographs to use [1,180]
N1=180;     %Starting angle for projection selection (0 is a good default)
conv=48;    %micrometer/pixel conversion value
StoO=220000;%Source to object distance [IN MICRONS]
OtoD=220000;%Object to detector distance [IN MICRONS]
emin=5;     %Minumum energy to consider (should = Sraw minimum energy)[KeV]
emax=50;    %Maximum energy to consider (should = Sraw maximum energy)[KeV]
degr=360;   %Number of degrees to include from input image (should be 360)
centx=477;  %Center X (right) pixel in the TRISO image (CUT0001 CURRENTLY)
centy=526;  %Center Y (down) pixel in the TRISO image (CUT0001 CURRENTLY)
centtop=403;%The Y pixel representing the top of the particle
centbot=645;%The Y pixel representing the bottom of the particle
srcx=512;   %X location of the source
srcy=512;   %Y location of the source
iter=8;     %Number of iterations to perform for the density calculation
ccrit=1E-6; %Allowed uncertainty between image and calculated values
Cbuff=3;    %Number of pixels adjacent to layer boundaries to ignore
Dbuff=3;    %Number of pixels adjacent to layer boundaries to ignore
Ebuff=3;    %Number of pixels adjacent to layer boundaries to ignore
Ecrop=.45;  %Fraction of data to crop from each end of the density data set
Dcrop=.45;  %Fraction of data to crop from each end of the density data set
Ccrop=.45;  %Fraction of data to crop from each end of the density data set
CDen=1.5;   %Initial guess for the density of layer C
DDen=1.5;   %Initial guess for the density of layer D
EDen=1.5;   %Initial guess for the density of layer E
%% RETRIEVAL OF RADIOGRAPHS AND RAW DATA%%
load('Sraw50.mat');%Energy spectrum data
load('U1cyl.mat');load('U2cyl.mat');load('U3cyl.mat');
load('U6cyl.mat');load('U7cyl.mat');%Raw attenaution data (cm^2/g)
main2=zeros(1024,1024,N);%PREALLOCATION
layers=zeros(1024,1024,N);%PREALLOCATION
for a=0:(N-1)%Loop over number of images
    img=sprintf('%04.0f',10*(N1+a*180/Ni));%Calculation and zero padding
    name=char(['G:\RESEARCH\MATLAB\CYLINDRICAL_TESTS\RAW_CYL3\CYL_50KVP'
num2str(img) '.tif']);%Char string
    nameLay=char(['G:\RESEARCH\MATLAB\CYLINDRICAL_TESTS\LAYERS3\LAY_50KVP'
num2str(img) '.tif']);%Char string
    main2(:,:,a+1)=imread(name);
    cut=imread(nameLay);
    layers(:,:,a+1)=cut(:,:,1);
end
%% CALCULATED CONSTANTS
Qsodist=StoO/conv;%Source to object distance in pixel units
Qoddist=OtoD/conv;%Object to detector distance in pixel units
magn=(Qsodist+Qoddist)/Qsodist;%Magnification based on imaging setup
[xsize,ysize]=size(main2(:,:,1));%size of the input image
binsz=Sraw(2,1)-Sraw(1,1);%Energy bin size calculation in KeV
S=(Sraw(:,2).*Sraw(:,1))';%Source particles * energy to get intensity
xind=1:1:xsize;xind=xind(ones(1,ysize),:);%Matrix containing X-index values
yind=xind';%Matrix containing Y-index values
IMcent=[centx,centy,Qsodist+Qoddist];%Center location of the fuel on the image
plane
SOloc=[srcx,srcy,0];%Location of the source
OBcent=SOloc+(IMcent-SOloc)/magn;
Z=zeros(xsize,ysize);%An image sized matrix of zeros for preallocating
%% ATTENUATION COEFFICIENT (cm^2/g) INTERPOLATION
Uraw={U1cyl U2cyl U3cyl U6cyl U7cyl};
for b=1:5
    for c=2:size(Uraw{b},1);                %Finds duplicate energies and
```

```
        if Uraw{b}(c-1,1)==Uraw{b}(c,1);       %adjusts to make them unique
           Uraw{b}(c-1,1)=Uraw{b}(c-1,1)-1E-9/c;%Assign unique energy vals.
        end
    end
    %Interpolation of attenuation coefficients
    Ulog=log10(Uraw{b}(:,2));                 %converts atten coeffs to log
    Uint=interp1(Uraw{b}(:,1),Ulog,binsz:binsz:225);%Interpolate
    Uraw{b}=10.^(Uint);                   %converts atten coeffs to linear
end
U1=Uraw{1}(emin/binsz:emax/binsz);%Cropped attenuation coefficients
U2=Uraw{2}(emin/binsz:emax/binsz);U3=Uraw{3}(emin/binsz:emax/binsz);
U4=Uraw{4}(emin/binsz:emax/binsz);U5=Uraw{5}(emin/binsz:emax/binsz);
%% THICKNESS DATA THETA-INTERPOLATION
Traw2=zeros(centbot-centtop+1,3,2*N);
for d=1:N
    Traw=layers(centtop:centbot,:,d);
    TS=(Traw==255);
    hbin=size(TS,1);
    TSpad=cat(2,TS,zeros(hbin,1));%Pad the right side of image
    TSpad2=cat(2,TSpad,zeros(hbin,1));%Pad the right side of image again
    TSshift=TSpad(:,2:end);%Shift a matrix one unit over
    TSshift2=TSpad2(:,3:end);%Shift a matrix two units over
    TS(TS==TSshift)=0;%If both matricies share a 1, one is removed
    TS(TS==TSshift2)=0;%If both matricies share a 1, one is removed
    TMAT=zeros(hbin,6);
    for e=1:hbin
        TMAT(e,:)=find(TS(e,:));
    end
    Traw2(:,:,d)=TMAT(:,4:6)-mean((TMAT(:,3)+TMAT(:,4))/2);
    Traw2(:,:,N+d)=-(TMAT(:,3:-1:1)-mean((TMAT(:,3)+TMAT(:,4))/2));
end
QoldH=(centtop:centbot)';
QnewH=(centtop:0.5:centbot)';
for p=1:3%Loop over layers
    for q=1:2*N%Loop over azimuthal cuts
        Traw3(:,p,q)=interp1(QoldH,Traw2(:,p,q),QnewH);%Interpolated Y-values
in pixel dimensions
    end
end
%% PATHLENGTH CALCULATION (MULTIPROJECTION INTERPOLATION)
%Determines the positions of the azimuthal cuts in the x-y coordinates
TDAT{5,N}=[];%DATA{5,2,N}=[];DAT2{5,2,N}=[];DAT3{5,2,N}=[];DAT4{5,2,N}=[];DAT5{
5,2,N}=[];%PREALLOCATION
for k=1%Loop over number of images
    Qazi=0:degr/(N*2)*4*atan(1)/180:degr*4*atan(1)/180;%Azimuthal angles for
slices
    Qnewazi=4*atan(1)/180*((0:45/960:degr));%New azi bin spacing
    %Qazi=Qazi(ones(size(QnewH)),:)-4*atan(1)/N*(k+1);%Repeating the matrix for
vectorization
    QrLAY2=zeros(size(QnewH,1),size(Qnewazi,2));
    for f=1:3%Loop over layers
        QrLAY=permute(Traw3(:,f,:),[1 3 2]);%One layer's radii for all azimuths
        QrLAY=cat(2,QrLAY,QrLAY(:,1));
        for m=1:size(QrLAY,1)
            QrLAY2(m,:)=interp1(Qazi,QrLAY(m,:),Qnewazi);%Interpolated Y-values
in pixel dimensions
        end
        QrLAY2=QrLAY2/magn;
        Qnewttamat=repmat(QnewH,size(Qnewazi));%Replicating newtta for use in
vectorized math
        Qnewazimat=repmat(Qnewazi,size(QnewH));%Replicating newazi for use in
vectorized math
```

```
        locX=QrLAY2.*cos(Qnewazimat)+OBcent(1);%Cylindrical to cartesian
conversion
        locY=repmat(SOloc(2)+(QnewH-SOloc(2))./magn,size(Qnewazi));%Cylindrical
to cartesian conversion
        locZ=QrLAY2.*sin(Qnewazimat)+OBcent(3);%Cylindrical to cartesian
conversion
        Qsrchalf=locZ<=Qsodist;Qdethalf=locZ>Qsodist;
        Qmapped1=Z;Qmapped2=Z;

        t1=(Qsodist+Qoddist)./locZ(Qsrchalf);%Parametric value to get from
source to detector
        projx1=round(srcx+(locX(Qsrchalf)-srcx).*t1);
        projy1=round(srcy+(locY(Qsrchalf)-srcy).*t1);
        projval1=((locX(Qsrchalf)-srcx).^2+(locY(Qsrchalf)-
srcy).^2+locZ(Qsrchalf).^2).^0.5;
        Qmapped1(projx1*ysize+projy1)=projval1;clear proj*

        t2=(Qsodist+Qoddist)./locZ(Qdethalf);%Parametric value to get from
source to detector
        projx2=round(srcx+(locX(Qdethalf)-srcx).*t2);
        projy2=round(srcy+(locY(Qdethalf)-srcy).*t2);
        projval2=((locX(Qdethalf)-srcx).^2+(locY(Qdethalf)-
srcy).^2+locZ(Qdethalf).^2).^0.5;
        Qmapped2(projx2*ysize+projy2)=projval2;clear proj*

        Qvalid=find(Qmapped2 & Qmapped1);
        PATHS=Z;
        PATHS(Qvalid)=Qmapped2(Qvalid)-Qmapped1(Qvalid);
        TDAT{f,k}=(PATHS)*conv/10000;%Storing matricies in cell array and
converting to cm

    end
    TDAT{2,k}=(TDAT{2,k}-TDAT{1,k});%Final thickness of layers in cm
    TDAT{3,k}=(TDAT{3,k}-TDAT{2,k}-TDAT{1,k});
    T1=TDAT{1,k};T2=TDAT{2,k};T3=TDAT{3,k};
toc
end
%axis ij
%detz=zeros(5);detz(:)=Qsodist+Qoddist;
%surf(locX,locY,locZ)
%hold
%surf([0:512:2048],[0:512:2048],detz)
%axis equal
%axis([0 2048 0 2048 0 Qsodist+Qoddist])

clear Q* Traw* loc*
%% DENSITY CALCULATION
main=main2(:,:,1);
dPLOT=Z;%PREALLOCATION
%Layer E
Elook2=double(T1==0 & T2==0 & T3>0 & yind>centtop & yind<centbot);
Elist=find(Elook2);%The indicies in the layer to be thinned out
Edown=Elist+Ebuff;Eup=Elist-Ebuff;Eleft=Elist-
ysize*Ebuff;Eright=Elist+ysize*Ebuff;%Perturbations
Elook2(Edown)=Elook2(Edown)+1;Elook2(Eup)=Elook2(Eup)+1;%Up and down
contributions
Elook2(Eleft)=Elook2(Eleft)+1;Elook2(Eright)=Elook2(Eright)+1;%Left and right
contributions
Elook=(Elook2==5);%Intersection of pixels to give the thinned region
%Actual Background Determination
    maincheck=double(medfilt2(main(:,:,k),[5 5]));%Filter to help determine
background
    %%%%%%
```

```
    blvl=mean(main(T3==0 & Elook2==0 & yind<=centx & yind<=(centtop-
100)));%Criteria for background pixel
    %%%%%%
    main=medfilt2(double(main(:,:,k))/blvl,[1 1]);%Scale gray levels into
percent penetration
EThic=T3(Elook);EThic=EThic(:,ones(1,(emax-emin)/binsz+1));%Thicknesses of the
layer
EGray=main(Elook);%Gray levels in the layer
EDens=ones(size(EGray));EDens(:)=EDen;%Initial density guesses
ECons=exp(-EThic.*U3(ones(size(EGray)),:));%Combination of thickness and
attenuation data
for l=1:iter%Number of Newton-Raphson iterations
    EIcalc=sum((S(ones(size(EGray)),:).*ECons.^EDens(:,ones(1,((emax-
emin)/binsz+1)))),2)./sum(S(ones(size(EGray)),:),2);%Prediction./(S(ones(size(E
Gray)),:).*EdetC.*EairC)

EdIcalc=sum((log(ECons).*S(ones(size(EGray)),:).*ECons.^EDens(:,ones(1,((emax-
emin)/binsz+1)))),2)./sum(S(ones(size(EGray)),:),2);%Derivative./(S(ones(size(E
Gray)),:).*EdetC.*EairC)
    EDens=EDens-((EIcalc-EGray)./EdIcalc);%Newton-Raphson iteration to get new
densities
    ENope=sum(abs(EIcalc-EGray)>ccrit);%Number of pixels that haven't converged
    if ENope==0;break;end%Exit criteria if all pixels converge
end
EPerc=ENope/size(EGray,1)*100;disp(sprintf('%0.2f%s',EPerc,'% of pixels in
layer E did not converge.'))
ESort=sort(EDens);ESort=ESort(round(size(EDens)*Ecrop):round(size(EDens)*(1-
Ecrop)));%Sort and crop
dE=mean(ESort);dPLOT(Elook)=EDens;%Determines density value and makes a density
plot
%clear E*
%Layer D
Dlook2=double(T1==0 & T2>0 & yind>centtop & yind<centbot);
Dlist=find(Dlook2);%The indicies in the layer to be thinned out
Ddown=Dlist+Dbuff;Dup=Dlist-Dbuff;Dleft=Dlist-
ysize*Dbuff;Dright=Dlist+ysize*Dbuff;%Perturbations
Dlook2(Ddown)=Dlook2(Ddown)+1;Dlook2(Dup)=Dlook2(Dup)+1;%Up and down
contributions
Dlook2(Dleft)=Dlook2(Dleft)+1;Dlook2(Dright)=Dlook2(Dright)+1;%Left and right
contributions
Dlook=(Dlook2==5);%Intersection of pixels to give the thinned region
DEThic=T3(Dlook);DEThic=DEThic(:,ones(1,(emax-emin)/binsz+1));%Thicknesses of
the layer
DThic=T2(Dlook);DThic=DThic(:,ones(1,(emax-emin)/binsz+1));%Thicknesses of the
layer
DGray=main(Dlook);%Gray levels in the layer
DDens=ones(size(DGray));DDens(:)=DDen;%Initial density guesses
DECons=exp(-DEThic.*U3(ones(size(DGray)),:)).^dE;%Combination of thickness and
attenuation data
DCons=exp(-DThic.*U2(ones(size(DGray)),:));%Combination of thickness and
attenuation data
for l=1:iter%Number of Newton-Raphson iterations
    DIcalc=sum(S(ones(size(DGray)),:).*DECons.*DCons.^DDens(:,ones(1,((emax-
emin)/binsz+1))),2)./sum(S(ones(size(DGray)),:),2);%Prediction

DdIcalc=sum(log(DCons).*S(ones(size(DGray)),:).*DECons.*DCons.^DDens(:,ones(1,(
(emax-emin)/binsz+1))),2)./sum(S(ones(size(DGray)),:),2);%Derivative
    DDens=DDens-((DIcalc-DGray)./DdIcalc);%Newton-Raphson iteration to get new
densities
    DNope=sum(abs(DIcalc-DGray)>ccrit);%Number of pixels that haven't converged
    if DNope==0;break;end%Exit criteria if all pixels converge
end
```

```
DPerc=DNope/size(DGray,1)*100;disp(sprintf('%0.2f%s',DPerc,'% of pixels in
layer D did not converge.'))
DSort=sort(DDens);DSort=DSort(round(size(DDens)*Dcrop):round(size(DDens)*(1-
Dcrop)));%Sort and crop
dD=mean(DSort);dPLOT(Dlook)=DDens;%Determines density value and makes a density
plot
clear D*
%Layer C
Clook2=double(T1>0 & yind>centtop & yind<centbot);
Clist=find(Clook2);%The indicies in the layer to be thinned out
Cdown=Clist+Cbuff;Cup=Clist-Cbuff;Cleft=Clist-
ysize*Cbuff;Cright=Clist+ysize*Cbuff;%Perturbations
Clook2(Cdown)=Clook2(Cdown)+1;Clook2(Cup)=Clook2(Cup)+1;%Up and down
contributions
Clook2(Cleft)=Clook2(Cleft)+1;Clook2(Cright)=Clook2(Cright)+1;%Left and right
contributions
Clook=(Clook2==5);%Intersection of pixels to give the thinned region
CEThic=T3(Clook);CEThic=CEThic(:,ones(1,(emax-emin)/binsz+1));%Thicknesses of
the layer
CDThic=T2(Clook);CDThic=CDThic(:,ones(1,(emax-emin)/binsz+1));%Thicknesses of
the layer
CThic=T1(Clook);CThic=CThic(:,ones(1,(emax-emin)/binsz+1));%Thicknesses of the
layer
CGray=main(Clook);%Gray levels in the layer
CDens=ones(size(CGray));CDens(:)=CDen;%Initial density guesses
CECons=exp(-CEThic.*U3(ones(size(CGray)),:)).^dE;%Combination of thickness and
attenuation data
CDCons=exp(-CDThic.*U2(ones(size(CGray)),:)).^dD;%Combination of thickness and
attenuation data
CCons=exp(-CThic.*U1(ones(size(CGray)),:));%Combination of thickness and
attenuation data
for l=1:iter%Number of Newton-Raphson iterations

CIcalc=sum(S(ones(size(CGray)),:).*CECons.*CDCons.*CCons.^CDens(:,ones(1,((emax
-emin)/binsz+1))),2)./sum(S(ones(size(CGray)),:),2);%Prediction

CdIcalc=sum(log(CCons).*S(ones(size(CGray)),:).*CECons.*CDCons.*CCons.^CDens(:,
ones(1,((emax-emin)/binsz+1))),2)./sum(S(ones(size(CGray)),:),2);%Derivative
    CDens=CDens-((CIcalc-CGray)./CdIcalc);%Newton-Raphson iteration to get new
densities
    CNope=sum(abs(CIcalc-CGray)>ccrit);%Number of pixels that haven't converged
    if CNope==0;break;end%Exit criteria if all pixels converge
end
CPerc=CNope/size(CGray,1)*100;disp(sprintf('%0.2f%s',CPerc,'% of pixels in
layer C did not converge.'))
CSort=sort(CDens);CSort=CSort(round(size(CDens)*Ccrop):round(size(CDens)*(1-
Ccrop)));%Sort and crop
dC=mean(CSort);dPLOT(Clook)=CDens;%Determines density value and makes a density
plot
%clear C*
toc
```

```
%Cone Geometry TRISO Image Generator
%Created by Frank Strantz
%In the algorithm, detector setup parameters and TRISO fuel measurements
%   are used to determine the gray levels of the resulting image.
%The Uraw matricies are lists of energy levels and corresponding
%   attenuation coefficients. Sraw is from Spekcalc.
%%%%%%%%%%%%%%%%%%%%%%%%%%%%%%%%%%%%%%%%%%%%%%%%%%%%%%%%%%%%%%%%%%%%%%%%%%%%%%%
clear all;clc;close all;tic
%% INPUT PARAMETERS
Ni=181;     %Total number of radiographs in sample set
N=4;        %Number of radiographs to use [1,180]
N1=0;       %Starting angle for projection selection (0 is a good default)
conv=0.56;  %micrometer/pixel conversion value
StoO=100000;%Source to object distance [IN MICRONS]
OtoD=10000; %Object to detector distance [IN MICRONS]
emin=2;     %Minumum energy to consider (should = Sraw minimum energy)[KeV]
emax=20;    %Maximum energy to consider (should = Sraw maximum energy)[KeV]
centx=939;  %Center X (right) pixel in the TRISO image (CUT0001 CURRENTLY)
centy=1060; %Center Y (down) pixel in the TRISO image (CUT0001 CURRENTLY)
R1=250;     %Radius of kernel (microns)
R2=345;     %Radius of buffer layer (microns)
R3=385;     %Radius of IPyC layer (microns)
R4=420;     %Radius of SiC layer (microns)
R5=460;     %Radius of OPyC layer (microns)
D1=10.97;   %Density of kernel (g/cm^3)
D2=1.1;     %Density of buffer layer (g/cm^3)
D3=1.9;     %Density of IPyC layer (g/cm^3)
D4=3.18;    %Density of SiC layer (g/cm^3)
D5=1.9;     %Density of OPyC layer (g/cm^3)
D6=.00122521;%Density of air (g/cm^3)
D7=4.51;    %Density of CsI(Tl) scintillator (g/cm^3)
Tscint=.05;%Scintillator thickness (cm)
xsize=2048; %X size of the image to be generated
ysize=2048; %Y size of the image to be generated
Sx=1024;    %X location of the source
Sy=1024;    %Ylocation of the source
Sz=0;       %Z location of the source
nvar=0.005;     %Variance of added Gaussian noise
%% RETRIEVAL OF RADIOGRAPHS AND RAW DATA%%
load('Sraw20.mat');%Energy spectrum data
load('U1raw.mat');load('U2raw.mat');load('U4raw.mat');load('U6raw.mat');load('U
7raw.mat');%Raw attenaution data (cm^2/g)
%% CALCULATED CONSTANTS
R=[R1;R2;R3;R4;R5]./conv;%Radii converted to pixel units
D=[D1;D2;D3;D4;D5;D6;D7];%Densities in g/cm^3
Qsodist=StoO/conv;%Source to object distance in pixel units
Qoddist=OtoD/conv;%Object to detector distance in pixel units
Qsddist=Qsodist+Qoddist;
magn=(Qsodist+Qoddist)/Qsodist;%Magnification based on imaging setup
binsz=Sraw(2,1)-Sraw(1,1);%Energy bin size calculation in KeV
S=(Sraw(:,2).*binsz.*Sraw(:,1))';%Source particles * energy to get intensity
xind=1:1:xsize;xind=xind(ones(1,ysize),:);%Matrix containing X-index values
yind=xind';%Matrix containing Y-index values
Qoffx=xind-xsize/2;Qoffy=yind-ysize/2;%Offset from the center positions
rays=(((Qoffx.^2+Qoffy.^2).^0.5).^2+(Qsodist+Qoddist).^2).^0.5;%Source to
detector distances
%angles=acos((Qsodist+Qoddist)./Qrays);%Angles from pixel to source to detector
center
Qraysx=(Qoffx.^2+(Qsodist+Qoddist).^2).^0.5;%Source to detector X distances
Qanglesx=acos((Qsodist+Qoddist)./Qraysx);%X component of angles
Qraysy=(Qoffy.^2+(Qsodist+Qoddist).^2).^0.5;%Source to detector Y distances
Qanglesy=acos((Qsodist+Qoddist)./Qraysy);%Y component of angles
Qtransx=Qoddist.*tan(Qanglesx);%The x displacement caused by the cone beam
```

```
Qtransx(:,1:end/2)=-1.*Qtransx(:,1:end/2);%Changing the sign of the left half
of data
Qtransy=Qoddist.*tan(Qanglesy);%The y displacement caused by the cone beam
Qtransy(1:end/2,:)=-1.*Qtransy(1:end/2,:);%Changing the sign of the upper half
of data
Qdispx=round(xind-Qtransx);%The displaced X position converting from detector
plane to particle plane
Qdispy=round(yind-Qtransy);%The displaced Y position converting from detector
plane to particle plane
Qxoffreal=xind-Qdispx(1,centx);%X-Offset from the particle center
Qyoffreal=yind-Qdispy(centy,1);%Y-Offset from the particle center
Z=zeros(xsize,ysize);%An image sized matrix of zeros for preallocating
%% ATTENUATION COEFFICIENT (cm^2/g) INTERPOLATION
Uraw={U1raw U2raw U2raw U4raw U2raw U6raw U7raw};
for b=1:7
    for c=2:size(Uraw{b},1);                  %Finds dupilcate energies and
        if Uraw{b}(c-1,1)==Uraw{b}(c,1);       %adjusts to make them unique
            Uraw{b}(c-1,1)=Uraw{b}(c-1,1)-1E-9/c;%Assign unique energy values
        end
    end
    %Interpolation of attenuation coefficients
    Ulog=log10(Uraw{b}(:,2));                 %converts atten coeffs to log
    Uint=interp1(Uraw{b}(:,1),Ulog,.001*binsz:.001*binsz:.225);%Interpolate
    Uraw{b}=10.^(Uint);                   %converts atten coeffs to linear
end
%%
T{1,7}=[];%Preallocation
A=(xind-Sx).^2+(yind-Sy).^2+(Qsddist-Sz).^2;%Quadratic equation coefficient
B=2*((xind-Sx).*(Sx-centx)+(yind-Sy).*(Sy-centy)+(Qsddist-Sz).*(Sz-
Qsodist));%Quadratic equation coefficient
for a=1:5
    r=R(a);
    C=centx.^2+centy.^2+Qsodist.^2+Sx.^2+Sy.^2+Sz.^2-
2.*(centx.*Sx+centy.*Sy+Qsodist.*Sz)-r.^2;%Quadratic equation coefficient
    Qsol1=real((-B+(B.^2-4.*A.*C).^0.5)./(2*A));%First solution
    Qsol2=real((-B-(B.^2-4.*A.*C).^0.5)./(2*A));%Second solution
    %The thickness is the magnitude of the distance between the two
    %intersections the line makes with the sphere
    Qthick=(conv/10000).*(((Qsol1-Qsol2).*(xind-Sx)).^2+((Qsol1-Qsol2).*(yind-
Sy)).^2+((Qsol1-Qsol2).*(Qsddist-Sz)).^2).^0.5;
    T{a}=Qthick;
end
clear Q* A B
T{2}=(T{2}-T{1});T{3}=(T{3}-T{2}-T{1});%Final thickness of layers in cm
T{4}=(T{4}-T{3}-T{2}-T{1});%Final thickness of layers in cm
T{6}=rays.*(conv/10000)-T{5};%Finding thickness of air
T{5}=(T{5}-T{4}-T{3}-T{2}-T{1});%Final thickness of layers in cm
T{7}=Z;T{7}(:)=Tscint;%Thickness of the scintillator
Ipoly=Z;%Preallocation
for c=1:(emax-emin)/binsz+1
    Imono=ones(size(Z));%Preallocation
    for b=1:6%Looping over materials
    Tene=exp(-T{b}.*Uraw{b}(c+emin/binsz-1).*D(b));
    Imono=Imono.*Tene;
    end
    Ipoly=Ipoly+S(c).*Imono.*(1-exp(-T{7}.*Uraw{7}(c+emin/binsz-1).*D(7)));
end
%clear Tene
I=Ipoly./sum(S);
I=imnoise(I,'gaussian',0,nvar);
imshow(I,[])
imwrite(I,char([num2str(emax) 'KVP_' num2str(nvar) 'VarNoise_' num2str(Tscint)
'ScintT.tiff']));toc
```

APPENDIX C.
IMAGING SYSTEM SPECIFICATIONS

Table C.1. X-ray sensor and generator specifications of the utilized system

X-ray Sensor Specifications	
Sensor Module	
Provider/part number	Rad-icon/RM1165-02
Sensor type	CMOS photodiode array
Interface	DVI
Scintillator screen material	Gd_2O_2S
Weight of sensor (kg)	0.8
X-ray energy range (KVp)	10-160
Dynamic range	4000:1
Max frame rate (Hz)	2.7
Pixels	1024x1024
Active area (mm)	49.3x49.2
Resolution (μm)	48
Average dark current (ADU/s)(1)	8
Conversion gain (elec/ADU)	500
Data rate (kHz)	1500
Readout period (ms)	370
Camera Module	
Provider	Rad-icon/RM1159-01
Resolution (bits)	12 or 14
Interface	High-speed parallel LVDS
X-ray Generator Specifications	
X-Ray Tube	
Provider/part number	Gulmay/HPX-225-11
Peak voltage (KVp)	225
Focal spot size (mm)	0.4 (small), 1.0 (large)
Target angle (degrees)	11
Inherent filtration (mm)	0.8 (Be)
Radiation coverage (degrees)	40 x 30
Maximum Continuous Rating (W)	800 (small), 1800 (large)
Filament current (amps)	4.1
X-Ray Generator	
Provider/part number	Gulmay/CP225
KV accuracy	±1%
mA range	0-30
Max power (W)	3200

BIBLIOGRAPHY

[1] Stansfield, O. M. "Evolution of HTGR Coated Particle Fuel Design." *Energy*, 1991: 33-45.

[2] Shulten, R. "Possible new Developments based on HTGR technology and operating experience." *IAEA bulletin*, 1989: 40-42.

[3] Verfondern, Karl, and Young-Woo Lee. "Advances in HTGR Fuel Technology - A New IAEA Coordinated Research Program." *International Congress on Advances in Nuclear Power Plants 2005.* Seoul: American Nuclear Society, 2005. 274-282.

[4] Pacific Northwest National Laboratory. *Innovative Approaches to Automating QA/QC of Fuel Particle Production Using On-Line Nondestructive Methods for Higher Reliability.* Richland: Pacific Northwest National Laboratory, 2004.

[5] Petti, D.A., J. Buongiorno, J.T. Maki, R.R. Hobbins, and G.K. Miller. "Key differences in the fabrication, irradiation and high temperature accident testing of US and German TRISO-coated particle fuel, and their implications on fuel performance." *Nuclear Engineering and Design*, 2003: 281-297.

[6] Idaho National Laboratory. "INL Portal." *Idaho National Laboratory: The Energy of Innovation.* May 24, 2010. https://inlportal.inl.gov/portal/server.pt/document/74489/module_2b_-_htgr_motivations___applications_pdf (accessed June 28, 2011).

[7] International Atomic Energy Agency. *Fuel performance and fission product behavior in gas cooled reactors.* Vienna: International Atomic Energy Agency, 1997.

[8] Lee, Young-Woo, Ji-Yeon Park, Yeon Ku Kim, Kyung Chae Jeong, Woong Ki Kim, Bong Goo Kim, Young Min Kim, and Moon Sung Cho. "Development of HTGR-coated particle fuel technology in Korea." *Nuclear Engineering and Design*, 2008: 2842-2853.

[9] Lopez-Honorato, E., P.J. Meadows, and P. Xiao. "Fluidized bed chamical vapor deposition of pyrolytic carbon - I. Effect of deposition conditions on microstructure." *Carbon*, 2009: 396-410.

[10] Katoh, Yutai, Lance Snead, Takashi Nozawa, Sosuke Kondo, and Jeremy Busby. "Thermophysical and mechanical properties of near-stoichiometric fiber CVI SiC/SiC composites after neutron irradiation at elevated temperatures." *Journal of Nuclear Materials*, 2010: 48-61.

[11] Snead, Lance, Takashi Nozawa, Yutai Katoh, Thak-Sang Byun, Sosuke Kondo, and David Petti. "Handbook of SiC properties for fuel performance modeling." *Journal of Nuclear Materials,* 2007: 329-377.

[12] Lopez-Honorato, E., J. Tan, P.J. Meadows, G. Marsh, and P. Xiao. "TRISO coated fuel particles with enhanced SiC properties." *Journal of Nuclear Materials*, 2009: 219-224.

[13] Hinoki, T., L. Snead, Y. Katoh, A. Hasegawa, T. Nozawa, and A. Kohyama. "The effect of high dose/high temperature irradiation on high purity fibers and their silicon carbide composites." *Journal of Nuclear Materials,* 2002: 1157-1162.

[14] Powers, Jeffery, and Brian Wirth. "A review of TRISO fuel performace models." *Journal of Nuclear Materials,* 2010: 74-82.

[15] Orlander, Donald R. *Fundamental Aspects of Nuclear Reactor Fuel Elements.* Springfield: Technical Information Center, Office of Public Affairs; Energy Research and Development Administration, 1976.

[16] Hannink, Ryan, Reiner Kuhr, and Tony Morris. "Public Acceptance of HTGR Technology." *Proceedings of the 4th International Topical Meeting on High Temperature Reactor Technology.* Washington DC: ASME, 2008. 1-8.

[17] Chinn, R.E. *Ceramography.* Materials Park: ASM International, 2002.

[18] Gulmay. *X-Ray Generators and X-Ray Controllers.* 2009. http://www.gulmay.co.uk/generators-over-2kw/cp-225-x-ray-generator.html (accessed 5 10, 2011).

[19] Wolbarst, Anthony Brinton. *Physics of Radiology Second Edition.* Madison: Medical Physics Publishing, 2005.

[20] Shultis, J. Kenneth, and Richard E. Faw. *Radiation Shielding.* La Grange Park: American Nuclear Society, Inc., 2000.

[21] Gonzalez, Rafael C., and Richard E. Woods. *Digital Image Processing Third Edition.* New Jersey: Pearson Prentice Hall, 2008.

[22] Tsoulfanidis, Nicholas. *Measurement and Detection of Radiation.* District of Columbia: Taylor & Francis, 1995.

[23] Berger, M.J., J.H. Hubbell, S.M. Seltzer, J. Chang, J.S. Coursey, R. Sukumar, D.S. Zucker, and K. Olsen. *XCOM: Photon Cross Sections Database.* Novermber 1, 2010. http://www.nist.gov/pml/data/xcom/index.cfm (accessed December 15, 2010).

[24] Poludniowski, G., G. Landry, F. Deblois, P.M. Evans, and F. Verhaegen. "SpekCalc: a program to calculate photon spectra from tungsten anode x-ray tubes." *Phys. Med. Biol.*, 2009: N433.

VITA

Frank Angelo Strantz was born in St. Paul, Minnesota. In May of 2010 he received his Bachelor of Science degree in Nuclear Engineering from Missouri University of Science and Technology. Frank's research activities have resulted in an American Nuclear Society conference paper.

Currently, he is working on his Master of Science degree in Nuclear Engineering at Missouri University of Science and Technology from which he will graduate in December 2011.